nature neuroscience

A new fate mapping system reveals context-dependent random or clonal expansion of microglia

Tuan Leng Tay[1], Dominic Mai[2], Jana Dautzenberg[1], Francisco Fernández-Klett[3], Gen Lin[4], Sagar[5], Moumita Datta[1], Anne Drougard[5], Thomas Stempfl[6], Alberto Ardura-Fabregat[1], Ori Staszewski[1], Anca Margineanu[7], Anje Sporbert[7], Lars M Steinmetz[4,8,9], J Andrew Pospisilik[5], Steffen Jung[10], Josef Priller[3,11], Dominic Grün[5], Olaf Ronneberger[2] & Marco Prinz[1,12]

Microglia constitute a highly specialized network of tissue-resident immune cells that is important for the control of tissue homeostasis and the resolution of diseases of the CNS. Little is known about how their spatial distribution is established and maintained *in vivo*. Here we establish a new multicolor fluorescence fate mapping system to monitor microglial dynamics during steady state and disease. Our findings suggest that microglia establish a dense network with regional differences, and the high regional turnover rates found challenge the universal concept of microglial longevity. Microglial self-renewal under steady state conditions constitutes a stochastic process. During pathology this randomness shifts to selected clonal microglial expansion. In the resolution phase, excess disease-associated microglia are removed by a dual mechanism of cell egress and apoptosis to re-establish the stable microglial network. This study unravels the dynamic yet discrete self-organization of mature microglia in the healthy and diseased CNS.

Microglia are the tissue macrophages of the CNS and, as such, are crucial for maintaining tissue homeostasis and for scavenging dying cells, pathogens and molecules through mechanisms both dependent on and independent of microbe-associated molecular pattern receptors[1–3]. Several recent genetic fate mapping approaches have clearly established the early embryonic origin of adult microglia[4–10]. There is now consensus that microglia, as well as perivascular and meningeal macrophages[11], are long-surviving and self-renewing populations of tissue macrophages in the CNS. However, many questions remain unanswered, in particular regarding the heterogeneity of microglia[12], the dynamics of microglial turnover[13] and the existence of a microglial stem cell population in the adult CNS[14–16]. Ajami *et al.*[17] and Mildner *et al.*[18,19] have used parabiotic and head-protected bone marrow chimeras, respectively, to demonstrate a lack of recruitment of peripheral myeloid cells into the CNS in the absence of a breach of the blood-brain barrier (BBB). *In vivo* imaging[20,21] and detailed histological analyses[22] supported the notion of evenly spaced distribution of nonactivated, ramified microglia under physiological conditions. Nevertheless, a direct method to demonstrate the vital dynamics of microglial cell expansion during health and disease is still lacking. Specifically, the studied unicolor reporter mouse models such as *Cx3cr1*^{GFP} (ref. 23), *Cx3cr1*^{creER}*R26R*^{DsRed} (which expresses a Cre recombinase and human estrogen receptor (ER) 1 (*ESR1*) fusion gene)[24] or *Cx3cr1*^{creER}*R26*^{YFP} (refs. 25–27) do not allow one to distinguish long-lived cells from ongoing replacement by daughter cells or to identify proliferative microglial niches or microglial precursors.

Here we established a new microglia-focused multicolor reporter system coupled with mathematical modeling that enabled us to visualize the profound ability of microglia to regulate their cell numbers in response to challenges in their microenvironment. Under steady state conditions, we found that different rates of random microglial cell proliferation correspond to the overall levels of proliferation in the surrounding region. In a model of acute neurodegeneration, microglia quickly shifted from random proliferation toward selected clonal expansion leading to clusters of daughter cells. We furthermore provide direct evidence for the restoration of the homeostatic microglial network by means of cell egress and apoptosis upon recovery. In sum, our results provide insight into the kinetics of the microglial network in health and disease.

RESULTS

Establishment of a new microglial fate mapping model

Microglial cells have been shown to self-replenish under steady state[6,8,28] or disease conditions[14,15,29–31]. However, the use of only a single genetic reporter for labeling the whole microglial population[23–25]

[1]Institute of Neuropathology, Faculty of Medicine, University of Freiburg, Freiburg, Germany. [2]Institute for Computer Science, University of Freiburg, Freiburg, Germany. [3]Department of Neuropsychiatry & Laboratory of Molecular Psychiatry, Charité – Universitätsmedizin Berlin, Berlin, Germany. [4]Genome Biology Unit, European Molecular Biology Laboratory, Heidelberg, Germany. [5]Max Planck Institute of Immunobiology and Epigenetics, Freiburg, Germany. [6]Center of Excellence for Fluorescent Bioanalytics, University of Regensburg, Regensburg, Germany. [7]Advanced Light Microscopy Technology Platform, Max Delbrück Center for Molecular Medicine, Berlin, Germany. [8]Department of Genetics, Stanford University School of Medicine, Stanford, California, USA. [9]Stanford Genome Technology Center, Palo Alto, California, USA. [10]Department of Immunology, Weizmann Institute of Science, Rehovot, Israel. [11]Cluster of Excellence 'NeuroCure', German Center for Neurodegenerative Diseases (DZNE) and Berlin Institute of Health (BIH), Berlin, Germany. [12]BIOSS Centre for Biological Signalling Studies, University of Freiburg, Freiburg, Germany. Correspondence should be addressed to T.L.T. (tuan.leng.tay@uniklinik-freiburg.de) or M.P. (marco.prinz@uniklinik-freiburg.de).

Received 24 May 2016; accepted 14 March 2017; published online 17 April 2017; doi:10.1038/nn.4547

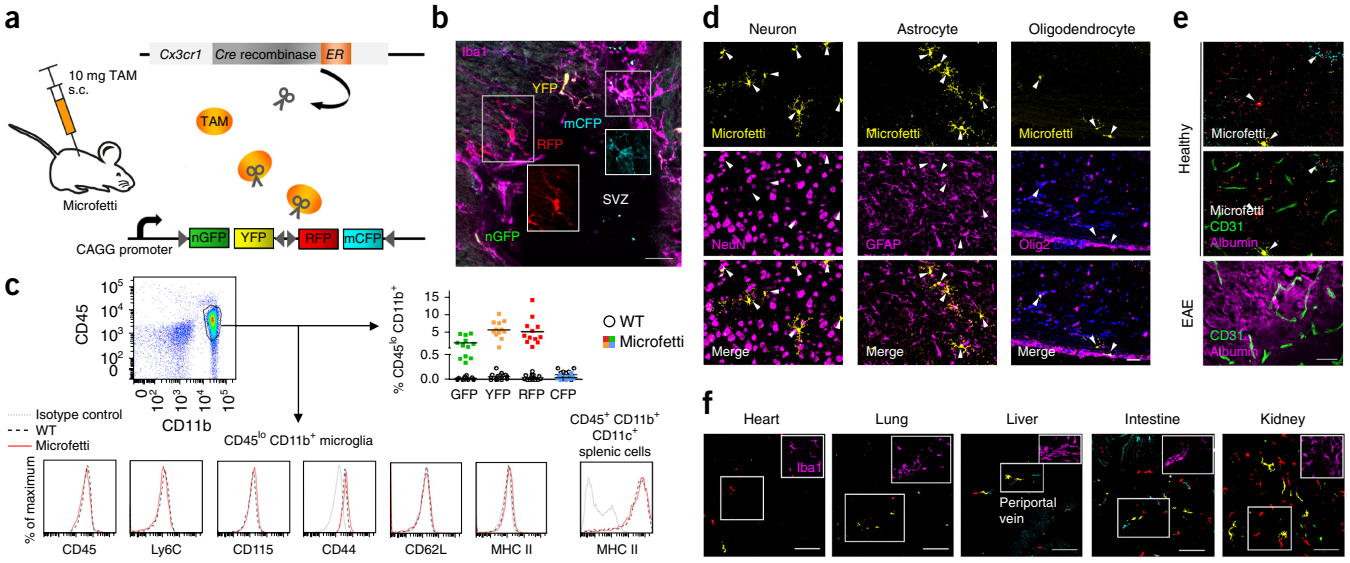

Figure 1 Characterization of the *Cx3cr1*^{creER}*R26R*^{Confetti} ('Microfetti') mouse model for fate mapping studies in microglia. (**a**) Illustration of the Microfetti model. Ten milligrams of tamoxifen (TAM) was given in a single subcutaneous (s.c.) injection to 8-week-old female Microfetti mice to induce Cre-mediated recombination that randomly produces one of four fluorescent reporter proteins in microglia. The scissors represent Cre recombinases that, upon binding of TAM, recognize and cut (or in addition flip) the reporter construct at *loxP* sites (triangles). This results in the expression of one color from each pair comprising nuclear GFP (nGFP, green) and cytoplasmic YFP (yellow), or cytoplasmic RFP (red) and membrane-tagged CFP (mCFP, cyan). Further TAM dosing is avoided to prevent flipping of the color pair. (**b**) Confetti-labeled Iba1$^+$ (magenta) microglia were detected as nGFP (green), YFP (yellow), RFP (red) and mCFP (cyan) label in the adult subventricular zone (SVZ). (**c**) Flow cytometric analysis of CD45^{lo} CD11b$^+$ microglia 10 d after TAM application. Top: quantification of Confetti label in microglia of Microfetti and non-transgenic wild-type mice. Each symbol (right) represents one mouse. $n = 12$ Microfetti and 14 wild type, pooled from three experiments. Bottom: flow cytometric quantification of microglial activation markers in Microfetti and wild type. Isotype controls are shown as gray lines. Representative histograms from four examined mice are shown. Splenic cells were used as positive control for MHC class II. (**d**) Confocal microscopy of the cortex of adult Microfetti mice 10 d after TAM application. Confetti expression was specific to microglia (false-colored yellow; CX_3CR1^+ Iba-1$^+$, as depicted in **b**) and was not detectable in nuclei of NeuN-positive neurons (left, magenta), glial fibrillary acidic protein (GFAP)-positive astrocytes (middle, magenta) or oligodendrocyte transcription factor (Olig)-2-positive oligodendrocytes (right, magenta). DAPI counterstain shows nuclei in the corpus callosum (right, blue). (**e**) Intact blood-brain barrier (top and middle) in TAM-treated Microfetti mice is revealed by the absence of serum albumin (magenta) extravasation from cortical blood vessels (CD31, green). Spinal cord with experimental autoimmune encephalomyelitis (EAE) served as positive control (bottom). (**f**) Confetti expression in CX_3CR1^+ Iba-1$^+$ tissue macrophages (magenta, insets) of Microfetti mice 1–3 weeks after TAM treatment. Scale bars, 30 µm in **b**, **d** and **e**, 100 µm in **f**.

does not allow one to study microglial dynamics over time, as it aggregates prevailing cells and their progeny as a single entity.

To distinguish microglial subsets in the brain parenchyma with multicolor reporters, we crossed the *Cx3cr1*^{creER} (refs. 25,26) and *R26R*^{Confetti} (ref. 32) mouse lines to generate *Cx3cr1*$^{creER/+}$ *R26R*$^{Confetti/+}$, a Confetti reporter strain that we termed "Microfetti." Upon application of tamoxifen (TAM) in *Cx3cr1*$^{creER/+}$ *R26R*$^{Confetti/+}$ mice, individual microglia can randomly express one of four possible fluorescent reporter proteins encoded by the Confetti construct: nuclear green fluorescent protein (nGFP), cytoplasmic yellow fluorescent protein (YFP), cytoplasmic red fluorescent protein (RFP), and membrane-tagged cyan fluorescent protein (mCFP) (**Fig. 1a**). Thus, we were able to tag long-lived tissue macrophages such as microglia in the CNS. Microglial cells marked by Confetti were phenotypically indistinguishable from non-transgenic wild-type microglia as shown by Iba-1 immunoreactivity (**Fig. 1b**) and the expression of myeloid markers (CD45, Ly-6C and CD115) and activation markers (CD44, CD62L and MHC class II) (**Fig. 1c**). The unaltered expression of myeloid surface markers between Confetti$^+$ and wild-type cells also holds true for circulating CX_3CR1^+ Ly-6C^{lo} monocytes within 10 d after TAM injection (**Supplementary Fig. 1a**). The labeling efficacy of approximately 14% is well-suited to studying microglial expansion dynamics in the brain as it provides sufficient spatial resolution[33]. As demonstrated by other studies, the unequal proportion of each reporter had no effect on our subsequent mathematical analyses[32–34]. Thorough histological analyses of other brain cells revealed no ectopic Confetti expression in neurons, astrocytes or oligodendrocytes (**Fig. 1d**). Notably, the BBB was not compromised in Microfetti mice (**Fig. 1e**). Varying amounts of Confetti expression were detected in CX_3CR1^+ Iba-1$^+$ macrophages in tissues such as heart, lung, liver, intestine and kidney (**Fig. 1f**).

We next optimized detection of the RFP signal for intravital multiphoton imaging via a cranial window to capture microglial cell division upon laser lesion *in vivo* over 2 d (**Supplementary Fig. 1b**). Comparison of the motility of microglial processes from *Cx3cr1*$^{GFP/+}$ mice with that of microglia from Microfetti mice did not show overt differences under steady state conditions, indicating that microglial multicolor labeling does not alter microglial surveillance behavior (**Supplementary Fig. 1c,d** and **Supplementary Videos 1** and **2**), and can therefore be employed for investigations of microglial dynamics *in vivo*.

The microglial network is largely stable during homeostasis

After having established a reliable microglial fate mapping system, we examined the kinetics of the microglial network at different time points after TAM induction (**Fig. 2a**). We analyzed Ly-6C^{lo} blood monocytes and CD45^{lo} CD11b$^+$ microglia in Microfetti mice in detail by flow cytometry over 36 weeks at defined time points (**Fig. 2b**). Due to their short half-life, monocytes rapidly lost their Confetti label after a few days whereas microglia remained stably tagged as expected[25,27].

Previously established labeling strategies for microglia using a single color[14,25] allow one neither to distinguish long-lived from constantly renewing microglial populations in the whole brain nor to examine the existence of any potential transient amplifying microglial progenitor cells[16] that may replenish the pool. To address these points, we acquired confocal volumes in six channels for the four native Confetti signals, Iba-1 immunoreactivity for microglia and 4′,6-diamidino-2-phenylindole (DAPI) nuclear counterstain (**Fig. 2c**) and analyzed many microglial cells in brain regions such as cortex, hippocampus and cerebellum over time (**Supplementary Table 1**). Nearest neighbor measurements between microglia implied region-correlated cell densities (**Supplementary Table 1**). The three-dimensional stacks were rendered and analyzed for the dynamics of the microglia network in different brain regions (**Fig. 2d** and **Supplementary Fig. 2a**). To establish the relationship between neighboring microglial cells, the proximities of each Confetti$^+$ microglial cell to each same-color cell in the three-dimensional volume were determined and compared to randomly generated distances based on 10,000 Monte Carlo (MC)-simulated outputs of each recorded data set (**Fig. 2e**). This procedure allowed us to infer whether same-color microglia were related as progeny of proliferation events or were located in the same neighborhood simply due to chance. We assigned observed measurements that lie above 98% of the MC data points to the former group and those below to the latter. For a clear overview of microglial network dynamics due to proliferation over time, we normalized all recorded versus MC comparisons (**Supplementary Fig. 2b**) and summarized the findings for each brain region (**Fig. 2f**). One to two microglial cell divisions were observed in the hippocampus and the cerebellum by 8 weeks after TAM treatment and continued to be detectable at 36 weeks, whereas the number of cortical Confetti$^+$ microglia remained largely unchanged over 36 weeks (**Fig. 2f** and **Supplementary Fig. 2b**). We furthermore established that these rare cell renewal events occurred in nonspecific positions within each brain compartment (**Supplementary Fig. 2c**). These data strongly suggest a considerable stability of the microglial network in the adult brain, especially in the cortex, and only subtle changes in the hippocampal and cerebellar regions.

Different regional microglial self-renewal and turnover rates

To extend our observations of environment-associated differences in the rate of microglial self-renewal, we took an additional approach, pulse-labeling actively dividing microglia in steady state. For this purpose, adult *Cx3cr1*$^{GFP/+}$ mice were injected with the thymidine analogs 5-ethynyl-2′-deoxyuridine (EdU), as a single dose, and subsequently 5-bromo-2′-deoxyuridine (BrdU) in five consecutive daily pulses (**Fig. 3a**). We used multiple doses of BrdU to accumulate the signals since cell proliferation during adult brain homeostasis is known to be low[8,28]. Any putative dividing CX_3CR1^+ microglial precursors present in proliferative niches should incorporate both analogs. We compared microglia to all other brain cells, such as GFAP$^+$ astrocytes and DCX$^+$ immature hippocampal neurons (**Fig. 3b–g**). No colocalization of EdU or BrdU with GFAP-immunolabeled astrocytes (**Fig. 3c**) was observed in the hippocampus, whereas we saw neural progenitor cells in the neurogenic niche triple-immunoreactive for DCX, EdU and BrdU (**Fig. 3d**,**g**). We next analyzed many GFP$^+$ parenchymal microglial cells and found region-specific rates of microglial proliferation in the cortex, hippocampus, hypothalamus, midbrain and cerebellum, and the highest rate of proliferation in the olfactory bulb (**Fig. 3h** and **Supplementary Table 2**). These values vary slightly from the [^{3}H]thymidine labeling indices of microglial proliferation in various brain regions described before[28], which might be due to the different techniques applied. Our results for the rates of microglial proliferation in the cortex, hippocampus and cerebellum of *Cx3cr1*$^{GFP/+}$ mice are in agreement with the findings on microglial network dynamics in Microfetti mice (**Fig. 2** and **Supplementary Fig. 2**). Furthermore, we identified low, intermediate and high microglial self-renewal in the midbrain, hypothalamus and olfactory bulb, respectively (**Fig. 3h** and **Supplementary Table 2**). Notably, the olfactory bulb was the only brain region where we detected highly proliferative EdU$^+$ BrdU$^+$ GFP$^+$ microglia that continuously renewed themselves within the time frame analyzed (**Fig. 3e,h**). However, neither multiple single Confetti$^+$ microglia nor clusters of them were observed in the olfactory bulb after several months in Microfetti mice during homeostasis (data not shown), suggesting an exceptionally high turnover of microglia in this distinct area. Based on the daily proliferation rates (**Supplementary Table 2**), microglia in different brain regions are estimated to completely turn over within 41 months in the cortex, 15 months in the hippocampus and as quickly as 8 months in the olfactory bulb. Considering that a mouse has an approximate lifespan of 2 years, these calculated rates point to three cycles of complete renewal of bulbar microglia, one to two cycles of hippocampal, hypothalamic and cerebellar microglial renewal, and the existence of long-lived microglia in the cortex and midbrain *in vivo*. Overall, the trend of regional differences of microglia self-renewal correlated with the proliferation of other CNS cells in the respective environment, albeit at a lower rate compared to that of other brain cells (**Fig. 3h**). We furthermore found no evidence for a designated proliferative microglial niche in the brain areas examined.

Confetti label recapitulates proliferation rates of unaltered microglia during homeostasis and disease

To examine whether Confetti reporter expression in microglia alters cell cycle kinetics, we compared the proliferation rates of Confetti$^+$ and Confetti$^-$ microglia from the cortex with microglia pooled from the olfactory bulb, hippocampus and cerebellum of the same animals (**Fig. 4**). To perform cytometric flow analysis of intracellular Ki67 immunoreactivity and identify Confetti$^+$ cells in the same experiment, we used an anti-GFP antibody for GFP, YFP and CFP, and an anti-RFP antibody. Notably, in both steady state (**Fig. 4a**) and lipopolysaccharide-induced cell activation (**Fig. 4b**), proliferation of microglia as indicated by the presence of Ki67 was comparable in Confetti$^+$ and Confetti$^-$ microglia. The percentages of Ki67$^+$ microglia recorded from steady state animals ($0.270 \pm 0.048\%$ and $0.406 \pm 0.057\%$ for cortical and pooled microglia from the olfactory bulb, hippocampus and cerebellum, respectively) are furthermore in support of our findings based on BrdU incorporation by microglia in various brain regions (**Supplementary Table 2**).

Selected clonal microglial expansion during CNS pathology

To investigate the kinetics of microgliosis during CNS pathology, we applied the unilateral facial nerve axotomy (FNX) model to Microfetti mice. The BBB remains intact in this procedure and remote neurodegeneration in the facial nucleus (FN) leads to local microglial activation without inducing an engraftment of circulating monocytes[18]. Two weeks after TAM treatment, we transected the facial nerve of Microfetti mice, leaving the unlesioned contralateral FN as an internal control (**Fig. 5a**). The fold changes in Iba-1$^+$ microglial cell density in the axotomized FN of Microfetti mice were consistent with those observed in the similarly axotomized FN of *Cx3cr1*$^{GFP/+}$ animals (**Fig. 5b** and **Supplementary Fig. 3a–c**). The increase in microglial cell number was specific to the FN, with only a minimal increase in microglia in the perinuclear zone bordering the FN at 7 d after

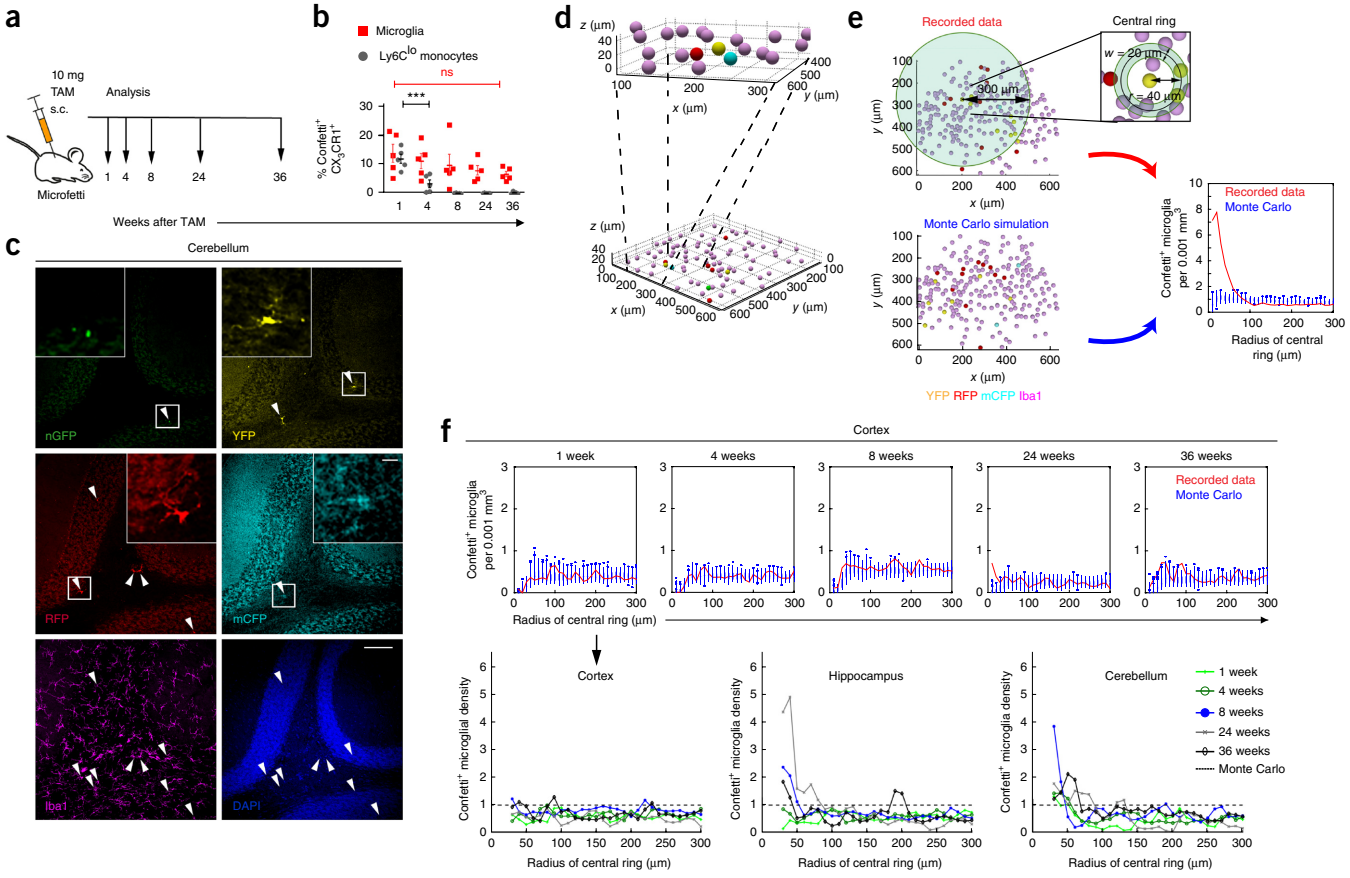

Figure 2 The microglial network is largely stable during homeostasis. (**a**) Scheme of analysis of Confetti$^+$ microglia after TAM treatment in 8-week-old female mice. (**b**) Flow cytometric analysis of Confetti expression in CX_3CR1^+ Ly-$6C^{lo}$ monocytes (gray) and CX_3CR1^+ $CD45^{lo}$ $CD11b^+$ microglia (red) at 1–36 weeks after TAM injection. See also **Supplementary Figure 1a**. Each symbol represents one mouse. One-way ANOVA, $***P < 0.001$; ns, not significant, $P = 0.0592$. (**c**) Representative maximum-intensity projection of a confocal stack from the cerebellum of an adult Microfetti mouse with native Confetti signals (arrowheads; nGFP, green; YFP, yellow; RFP, red; mCFP, cyan), Iba-1 immunolabeled microglia (magenta) and DAPI nuclear stain (blue). Scale bars, 10 µm (inset), 100 µm (main panels). (**d**) Three-dimensional rendering of confocal stack in **c** with colored spheres representing each microglial cell. (**e**) Strategy for computational analyses of Confetti$^+$ microglial distribution in this study. For every Confetti$^+$ microglial cell in every confocal stack (top left), Confetti$^+$ microglial cell density in concentric rings of 20 µm width (*w*) and radii (*r*) from 10 to 300 µm were measured. An example of a central ring with 40 µm radius is shown (top right). The largest radius ($r = 300$ µm) takes into account the maximum detectable migratory distance of 600 µm potentially traveled by a daughter cell after a division event. Monte Carlo (MC) simulation (bottom left) of random distribution of Confetti$^+$ microglial cells was performed 10,000 times for each data set to establish a baseline for microglial densities that may arise due to chance. Microglial density (*y* axis) was obtained by dividing same-color cell counts by ring volume of each ring size (*x* axis) (graph, bottom right). Mean cell densities from recorded stacks (red line) were compared to corresponding MC simulations (blue box plots represent density distributions: central mark is the median, box represents the 25th to 75th percentiles, whiskers extend to the 98th percentile and data points above were regarded as outliers. This example shows data from the injury model, where microglial proliferation is high, in order to illustrate a clear distinction between nonrandom cluster behavior and MC simulation. Measured values (red line) that lie above the 98th percentile of MC modeling (blue whiskers) identify nonchance occurrence of same-color Confetti$^+$ microglial cells and thus imply that proliferation has taken place. (**f**) Comparison of microglial proliferation based on Confetti$^+$ microglial density in different brain regions over time. Top, cortical microglial densities from recordings (red line) at each time point compared to results obtained from MC simulation (blue box plots). Bottom, Confetti$^+$ microglial densities were normalized to the 98th percentile of MC values from each time point to visualize proliferation events for the cortex, hippocampus and cerebellum over time. Down-arrow indicates normalization of cortical microglial densities (top) to a single graph (bottom left). Graphs are shown starting from 30 µm central ring radius based on measured NN distances in **Supplementary Table 1**. Relative microglial densities (*y* axis, ratio) calculated for the hippocampus and cerebellum at 8, 24 and 36 weeks lie above MC data points (normalized to 1) for central ring radii between 30 µm and 100 µm, indicating that proliferation began from between 4 and 8 weeks after TAM treatment. Mean data are shown. $n = 5$ mice per group. See also **Supplementary Figure 2**.

FNX (**Supplementary Fig. 3b**). In contrast, the more distant region containing the α part of the parvicellular reticular nucleus (PCRtA) and the unlesioned contralateral FN were devoid of any microgliosis (**Supplementary Fig. 3b**). Ki67$^+$ proliferating microglia were detectable in the FN only before the peak of microgliosis at 2 d after FNX (**Fig. 5c** and **Supplementary Fig. 3d,e**). From 2 to 14 d after FNX, microglia in the axotomized FN displayed an activated rod-like or amoeboid morphology accompanied by MHC class II expression, indicating microglial activation (**Supplementary Fig. 3f,g**). By 60 d, partial to complete recovery of impaired whisker movement was observed clinically in the mice, concomitant with an even distribution of microglia in the axotomized FN that had reacquired a ramified morphology and showed no signs of proliferation or activation, like those in the contralateral, unlesioned side (**Supplementary Fig. 3c–g**). We applied microglial cell cluster analysis to investigate the spatiotemporal dynamics of the microglial network following FNX (**Fig. 5d–f** and **Supplementary Table 3**). Clonal expansion of microglia resulting in increased microglial density and reduced intercellular distances

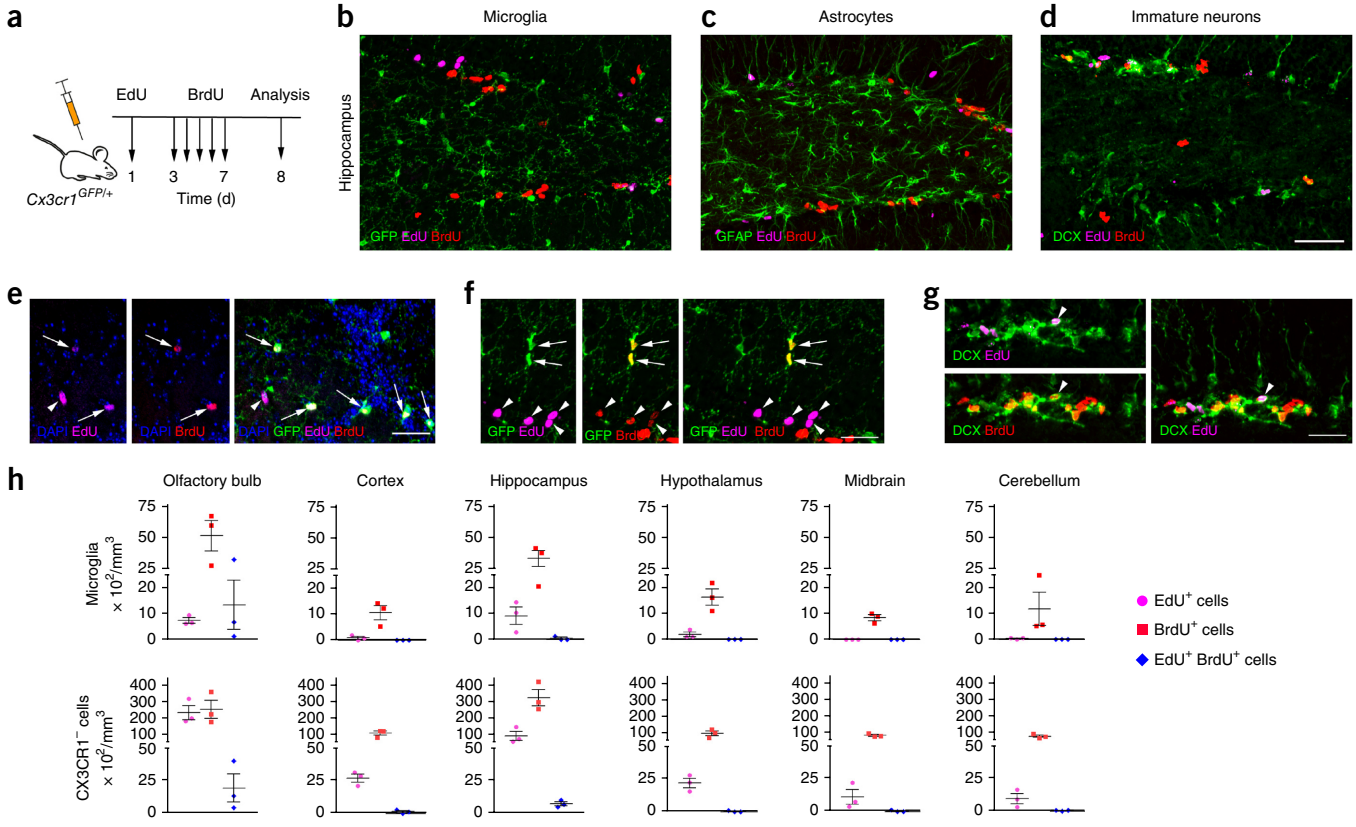

Figure 3 Regional difference of random microglial self-renewal. (**a**) Scheme of EdU and BrdU labeling in 13-week-old female *Cx3cr1*$^{GFP/+}$ mice to track microglial proliferation at steady state. (**b**–**d**) Representative confocal images of *Cx3cr1*$^{GFP/+}$ mice treated with EdU and BrdU show the distribution of EdU (magenta), BrdU (red) and (**b**) anti-GFP-labeled microglia (green), (**c**) anti-GFAP-labeled astrocytes (green), and (**d**) anti-DCX-labeled immature neurons (green) in the hippocampus. (**e**–**g**) Colocalization of EdU and/or BrdU with (**e**) bulbar and (**f**) hippocampal microglia, and with (**g**) DCX$^+$ neurons in the hippocampus. Arrows point to EdU$^+$ and/or BrdU$^+$ microglia (**e**,**f**). Arrowheads highlight EdU$^+$ and/or BrdU$^+$ CX_3CR1^- cells (**e**,**f**) and a triple-positive DCX$^+$ neuron (**g**). (**h**) Quantification of CX_3CR1^+ GFP$^+$ microglial (top) and CX_3CR1^- nonmicroglial (bottom) cells that colocalized with EdU (magenta), BrdU (red), or both (blue) in each brain region. Data are represented as mean ± s.e.m. in **h**. $n = 3$ mice. Scale bars, 50 µm in **d** (same scale in **b** and **c**), 30 µm in **e**–**g**.

(by measuring the nearest neighbor cell distances) occurred as early as 2 d, with daughter cells persisting up to 30 d after FNX (**Fig. 5f** and **Supplementary Table 3**). In comparison, the numbers of total Iba-1$^+$ microglia and nearest neighbor distances in the contralateral nucleus were similar across all stages (**Supplementary Table 3**). The occurrence of Confetti$^+$ microglia in the control nucleus was random throughout the experiment (**Fig. 5d,f**). The distribution of ipsilateral Confetti$^+$ microglia also tended toward randomness during the recovery phase at 60 d after FNX (**Fig. 5f**).

To achieve the sevenfold increase in microglial cell number observed from 2 to 7 d after FNX (**Fig. 5b,d** and **Supplementary Table 3**) without immigration of microglial cells into the FN, three divisions would have to take place for every existing microglial cell. We therefore studied the frequency distribution of different sizes of same-color Confetti$^+$ microglial clusters (**Fig. 5g**). Comparing the start of microglial doubling (2 d) with the peak of microgliosis (14 d), we found that clones comprising ≥4 cells were only observed at the latter stage (**Fig. 5g**). Thus, we conclude that local clonal expansion is sufficient to support the total microglial cell density at peak of microgliosis after FNX. In fact, any potential contribution of Confetti$^+$ microglia migrating from other CNS regions into the FN would lead to a more random distribution of these cells. The even distribution of such clusters throughout the FN further argues against the presence of specialized microglial progenitors. These data suggest that CNS pathology shifts from random self-renewal of the microglial network toward a rapid expansion of selected microglial clones. In this fast process of microgliosis, virtually every microglial cell has the chance to expand clonally.

Re-establishment of the microglial network by cell egress and cell death during the recovery phase

We observed a remarkable decrease in microglial density in the recovering FN (**Fig. 5** and **Supplementary Fig. 3**). What is the fate of the surplus microglia that accumulate during microgliosis? We first investigated whether there is a preference for retaining pre-existing or newly proliferated microglial cells. GFP$^+$ microglial cells that divided during the first 3 d after FNX were labeled with EdU and quantified at peak of injury (7 d) and at recovery (60 d) (**Fig. 6a–c**). We detected similar percentages of daughter cells (22.38 ± 2.93% at 7 d and 22.33 ± 3.14% at 60 d). Furthermore, at 60 d we observed the presence of EdU$^+$ GFP$^+$ microglia limited to the ventral pontine area, at some distance from the axotomized ipsilateral FN; these were absent from the same location 7 d after FNX (**Supplementary Fig. 4**). This suggests that microglial egress takes place during the resolution of microglial clusters.

To achieve broad coverage of the entire pontine region in order to uncover the fate of excess microglia, we established a method for high-throughput imaging with sufficient resolution for semiautomatic microglial cell detection in Microfetti mice after unilateral FNX (**Fig. 6d**). For the quantification of Confetti$^+$ Iba-1$^+$ microglial densities on the ipsilateral and contralateral sides, we further divided the large

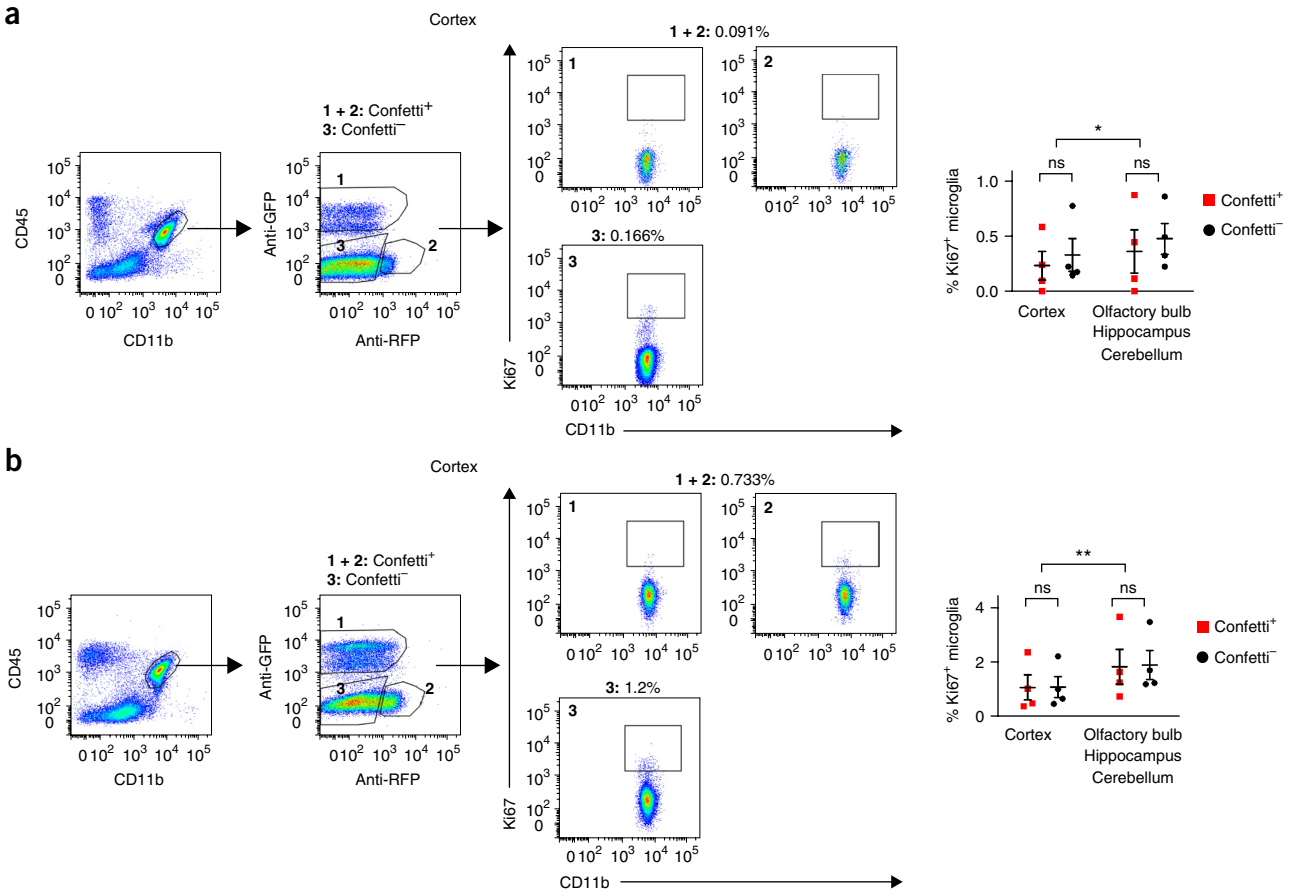

Figure 4 Detection of microglial proliferation in steady state and disease is independent of Confetti label. (**a**,**b**) Flow cytometric analysis of microglial proliferation. Total microglia from cortical fractions or pooled fractions from olfactory bulb, hippocampus and cerebellum were identified by CD45^{lo} CD11b^{+} profile and gated for Confetti expression (gates 1 and 2, labeled by anti-GFP antibody for GFP, YFP and CFP and anti-RFP antibody for RFP, respectively) and Confetti^{-} microglia (gate 3). Microfetti animals were TAM treated at 16–17 weeks of age. Intracellular stain for Ki67 identified proliferating microglia during steady state (**a**) and upon peripheral introduction of lipopolysaccharide 8 weeks after TAM treatment (**b**). Representative flow cytometric dot plots from the cortex are shown. Data are represented as mean ± s.e.m. Two-way ANOVA matched for subject, $^{*}P = 0.0346$, $^{**}P = 0.0053$; ns, not significant, $P = 0.866$ in **a**, $P = 0.871$ in **b**. $n = 4$ mice per group.

area of interest into three regions: (i) the gigantocellular reticular nucleus, (ii) intermediate reticular nucleus and PCRtA, and (iii) oral part of the spinal trigeminal nucleus (**Fig. 6d–f**). Interestingly, there was a small but significant difference in the fraction of Confetti^{+} Iba-1^{+} microglia in the gigantocellular reticular nucleus, intermediate reticular nucleus and PCRtA nuclei at 60 d after-FNX but not earlier (**Fig. 6e**). Qualitatively, these differences only consisted of one or two small standalone patches of Confetti^{+} Iba-1^{+} microglia per section (**Fig. 6f**). The nonsignificant scores from the MC-based Confetti^{+} microglial density analysis of the entire pons excluding the FN further emphasized the subtlety of these changes during recovery (data not shown).

We next used TUNEL labeling to examine the cell death kinetics of Iba-1^{+} microglia after FNX in Microfetti mice, as apoptosis is another possibility for eliminating excess microglia in the lesioned ipsilateral FN (**Fig. 6g,h**). The gradual increase in the mean rate of microglial apoptosis at 30 d (0.14 ± 0.19%) and 60 d (3.51 ± 3%) after FNX indicated that microglial apoptosis contributes to the elimination of excess microglia. There was generally higher phagocytic activity in the axotomized FN compared to the unlesioned contralateral side as indicated by stronger Lamp2 immunohistochemistry in Iba-1^{+} microglia (**Fig. 6i**). We identified actively phagocytosing microglia with phagocytic cups in the ipsilateral intermediate reticular and PCRtA nuclei 60 d after FNX (**Fig. 6j,k**). Assuming that the resolution of injury begins about 1 month after axotomy, daily low rates of apoptosis and outward movement of microglial cells are sufficient to return the number of cells in the lesioned ipsilateral FN to steady state by 60 d after FNX. Taken together, our data strongly suggest a dual mechanism of microglial cell removal for the restoration of the homeostatic microglial network after FNX: first, random inconspicuous egress of excess microglia from the area of CNS pathology into nearby compartments and, second, their local cell death by apoptosis.

Increase in cell migration, interferon response and lipid mediation accompany the resolution of microgliosis

Which molecular events take place during the progression of neural injury? To examine the transcriptional changes that accompany microglial clonal expansion in the axotomized FN, we isolated either the whole ventral pons or bulk microglia of both FNs for RNA sequencing (**Fig. 7a**). We first analyzed the ventral pons with the aim of identifying complementary signals from microglia and their mostly neuronal environment. We uncovered 1,344 significantly regulated genes that formed six clusters by comparing the axotomized side to the contralateral side at 7, 14 and 30 d after FNX (**Fig. 7b**). There was no difference in gene regulation between ipsilateral and contralateral sides by 60 d after FNX (data not shown), which is in line with the random

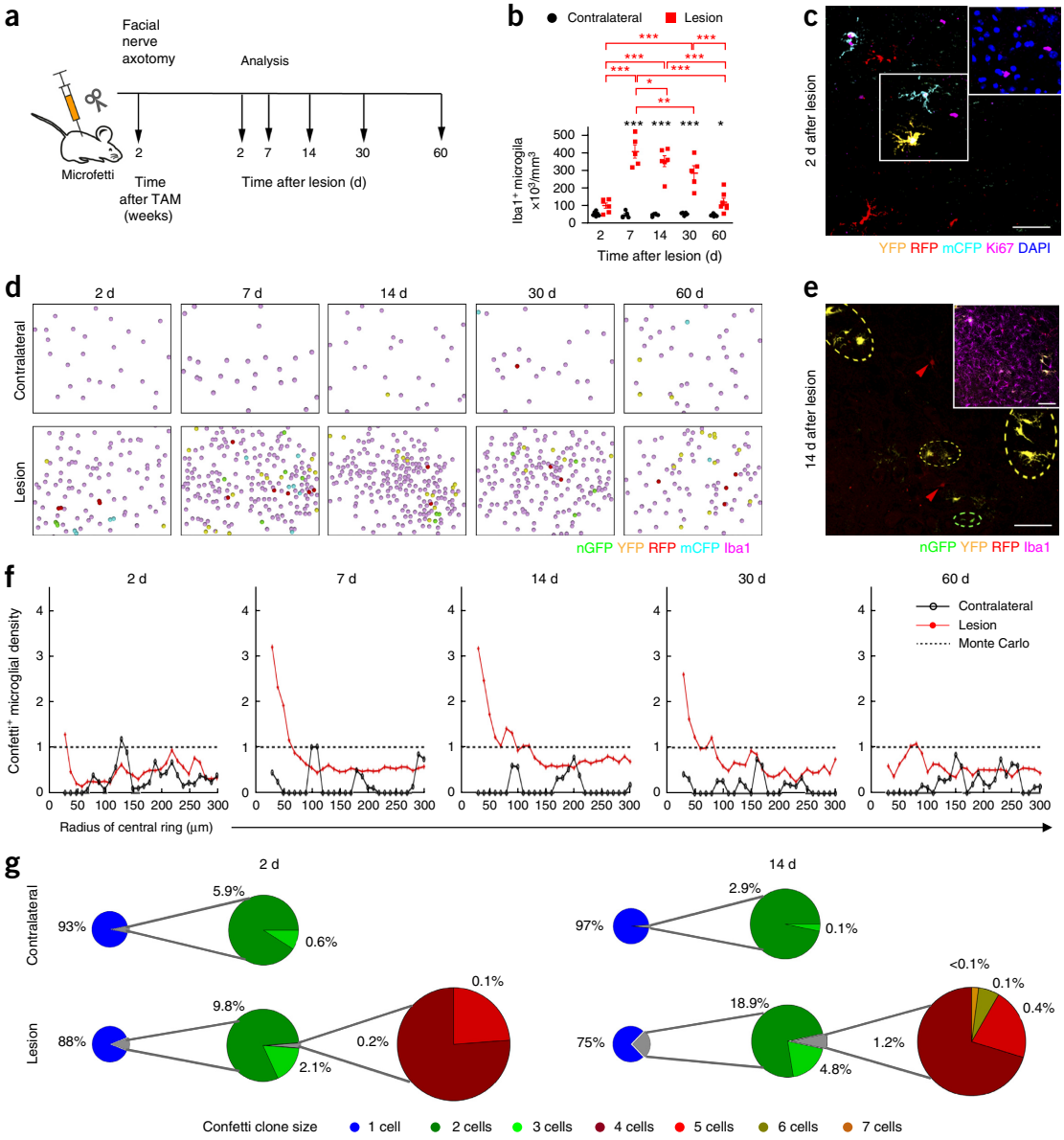

Figure 5 Clonal expansion of microglia upon injury revealed by spatiotemporal cluster analysis. (**a**) Scheme of microglial expansion analysis in the FN of TAM-treated Microfetti mice (8–9 weeks old) after FNX. (**b**) Quantification of Iba-1$^+$ microglia from onset (2 d after lesion) to peak (7 and 14 d) and then to resolution of injury (30 and 60 d). (**c**) Representative confocal image of proliferating Confetti$^+$ microglial cells (YFP, yellow and CFP, cyan) in the injured FN 2 d after lesion, labeled by Ki67 (magenta). Ki67 and DAPI (blue) nuclear counterstain, inset. (**d**) Representative two-dimensional renderings of Confetti$^+$ (green, yellow, red and cyan) and Iba-1 immunolabeled (magenta) microglia in matched lesioned and contralateral FN over the progression of injury. (**e**) Representative confocal image of clustered (ovals) and single (arrowheads) Confetti$^+$ microglial cells (nGFP, green; YFP, yellow; RFP, red) in the injured FN 14 d after lesion. Inset shows merge with Iba-1 immunolabel (magenta). (**f**) Comparison of Confetti$^+$ microglial proliferation following FNX in contralateral and injured FN. Microglial densities from confocal recordings were normalized to the 98th percentile of MC values (dotted line) derived for each data set (as described in **Fig. 2e,f**) and depicted here for the contralateral (black) and lesion (red) sides over the progression of injury. Graphs are shown starting from 30 µm central ring radius based on NN distances in **Supplementary Table 3**. Relative microglial densities (*y* axis, ratio) in the lesion side at 7, 14 and 30 d lie above MC data points (normalized to 1), indicating that same-color Confetti$^+$ microglia were derived from earlier proliferation events. (**g**) Distribution of Confetti$^+$ microglial clone sizes at 2 d and 14 d after FNX. For every Confetti$^+$ microglial cell, the number of same-color cells was counted for every concentric ring (used for the analysis detailed in **Fig. 2e**) to obtain a distribution of cluster sizes. The average of all distributions calculated using every concentric ring is shown. Clone sizes are indicated by different colors. One cell represents the absence of another Confetti$^+$ cell in a ring of a given radius. The biggest clones observed contained six or seven Confetti$^+$ microglia and were only detected in injured FN at the peak of microgliosis. Mean data are shown in **b** (± s.e.m.; two-way ANOVA, $^*P = 0.0114$ in red, 0.0116 in black, $^{**}P = 0.00556$, $^{***}P < 0.001$), **f** and **g**. $n = 6$ (2 d), 5 (7 d), 6 (14 d), 6 (30 d) and 7 (60 d) mice pooled from two experiments. Scale bars, 50 µm in **c** and **e**.

Confetti$^+$ microglial distribution at this time point (**Fig. 5f**). The most altered biological functions we found in total ventral pons after FNX included phagocytosis, immune response, antigen processing and presentation (cluster 1) and cell migration (cluster 5), which could be attributed mainly to the changes in microglia (**Fig. 7b**). Furthermore, the significant regulation of genes related to neuronal functions such as dendrite morphogenesis, axonogenesis (cluster 2), neuron death (cluster 3), synaptic transmission, neuron projection,

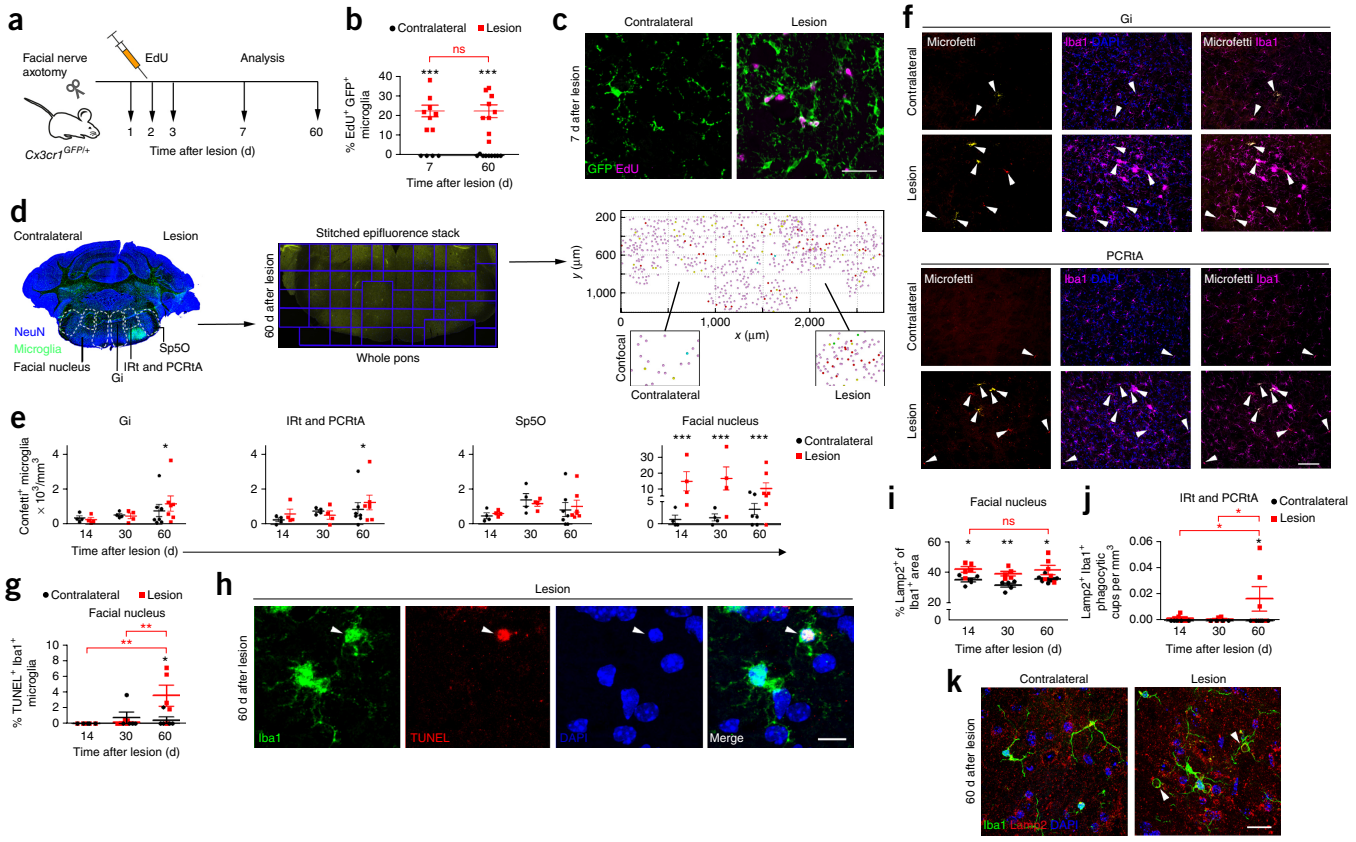

Figure 6 Reestablishment of the microglial network is achieved by egress and cell death during resolution of neurodegeneration. (**a**) Scheme of EdU application to 8-week-old female *Cx3cr1*$^{GFP/+}$ mice after facial nerve transection to track the fate of microglial cells that arose from injury-induced proliferation. (**b**) Percentage of EdU$^+$ GFP$^+$ microglial cells at peak of microgliosis (7 d) and recovery (60 d) after lesion. Each symbol represents one count. $n = 8$ (7 d) and 9 (60 d) mice pooled from two experiments. Two-way ANOVA revealed no difference among time points after lesion; ns, not significant, $P = 0.988$, $^{***}P < 0.0001$. (**c**) Representative confocal images for **b**. (**d**) Scheme for the analysis of Confetti$^+$ microglial distribution in pontine nuclei surrounding the ipsilateral and contralateral FN (left) in a random subset of sections analyzed in **Figure 5** from 14 to 60 d after lesion. Gi, gigantocellular reticular nucleus; IRt, intermediate reticular nucleus; PCRtA, parvicellular reticular nucleus α part; Sp5O, spinal trigeminal nucleus oral part. Stacks of whole pons imaged on an epifluorescence microscope were stitched using XuvTools (middle) for cell detection, computational rendering and region-specific calculations (right). Confocal volumes of FN are from the analysis shown in **Figure 5**. (**e**) Quantification of **d**. $n = 4$ (14 d), 4 (30 d) and 7 (60 d) mice pooled from two experiments. Confetti$^+$ microglial cell counts for FN from corresponding confocal volumes are shown here for comparison. Wilcoxon signed-rank test, $^*P = 0.0234$, 0.0234, $^{***}P < 0.001$. (**f**) Representative confocal images for **e**. Arrowheads indicate Confetti$^+$ Iba-1$^+$ microglial cells. (**g**) Percentage of TUNEL$^+$ Iba-1$^+$ microglia from the FN of Microfetti mice analyzed in **Figure 5** from 14 to 60 d after lesion. Each symbol represents mean count per animal. $n = 5$ mice per group. Two-way ANOVA revealed significant difference between time points after lesion and between the two FN at 60 d after injury, $^*P = 0.0199$, $^{**}P = 0.00239$, 0.00189 (top to bottom). (**h**) Representative confocal images for **g**. Arrowhead indicates a TUNEL$^+$ Iba-1$^+$ DAPI$^+$ microglial cell. (**i**) Percentage of Lamp2 coverage within Iba-1$^+$ microglia from the FN of Microfetti mice corresponding to **g**. Lamp2 and Iba-1 signals were automatically thresholded in each image plane for the measurement of the respective areas covered. Each symbol represents mean count per animal. $n = 5$ (14 d), 5 (30 d) and 6 (60 d) mice. Two-way ANOVA revealed no significant change between time points after lesion (ns, not significant, $P = 0.291$), but significant difference between the two FN, $^*P = 0.0155$, 0.0149, $^{**}P = 0.00785$. (**j**) Quantification of Lamp2$^+$ Iba-1$^+$ microglial phagocytic cups in the IRt and PCRtA nuclei. Phagocytic cups were identified as circular, 5–10 µm diameter Lamp2$^+$ Iba-1$^+$ structures. Each symbol represents mean count per animal. $n = 5$ (14 d), 5 (30 d) and 6 (60 d) mice. Two-way ANOVA showed significant difference between time points after lesion and significant difference between ipsilateral and contralateral sides only at 60 d after injury, $^*P = 0.0264$, 0.0329, 0.0152 (top to bottom). (**k**) Representative images for **j**. Arrowheads indicate Lamp2$^+$ Iba-1$^+$ microglial phagocytic cups. Data are represented as mean ± s.e.m. in **b**, **e**, **g**, **i** and **j**. Scale bars, 30 µm in **c**, 100 µm in **f**, 10 µm in **h**, 20 µm in **k**.

and cellular calcium ion homeostasis (cluster 4) are likely molecular indications of acute neurodegeneration (**Fig. 7b**). Downregulated neuron-related genes returned to baseline levels by 30 d (clusters 2 and 4, **Fig. 7b**). To specify the source of differential gene regulation at a cellular level, we examined transcriptomic data from FACS-sorted bulk microglia (**Fig. 7a,c**). We found in total 257 differentially expressed genes from 0 to 30 d in the lesion compared to the contralateral side (**Fig. 7c**). Gene induction was accompanied by obvious morphological changes in microglia (**Fig. 5** and **Supplementary Fig. 3**). Isolated microglia showed less transcriptomic changes compared to the whole ventral pons, indicating nonmicroglial environmental changes upon FNX (**Fig. 7b,c**). At the peak of microgliosis (7 d after FNX), the most strongly upregulated genes were related to biological functions involving protein translation and innate immune response in cluster 1 (**Fig. 7c,d**). Furthermore, at 30 d we observed an upregulation of genes related to migration, inflammatory response, lipid mediation and calcium-mediated signaling, and negative regulation of cell proliferation genes that belonged to clusters 2 and 4 (**Fig. 7c,d**). A total of 63 genes, including genes related to interferon response, lipid mediation, the MHC class I complex and translation, were found to be differentially regulated (up and down) between 7 and 30 d in the lesioned FN (**Fig. 7d**). The increased regulation of these functions at 30 d paralleled

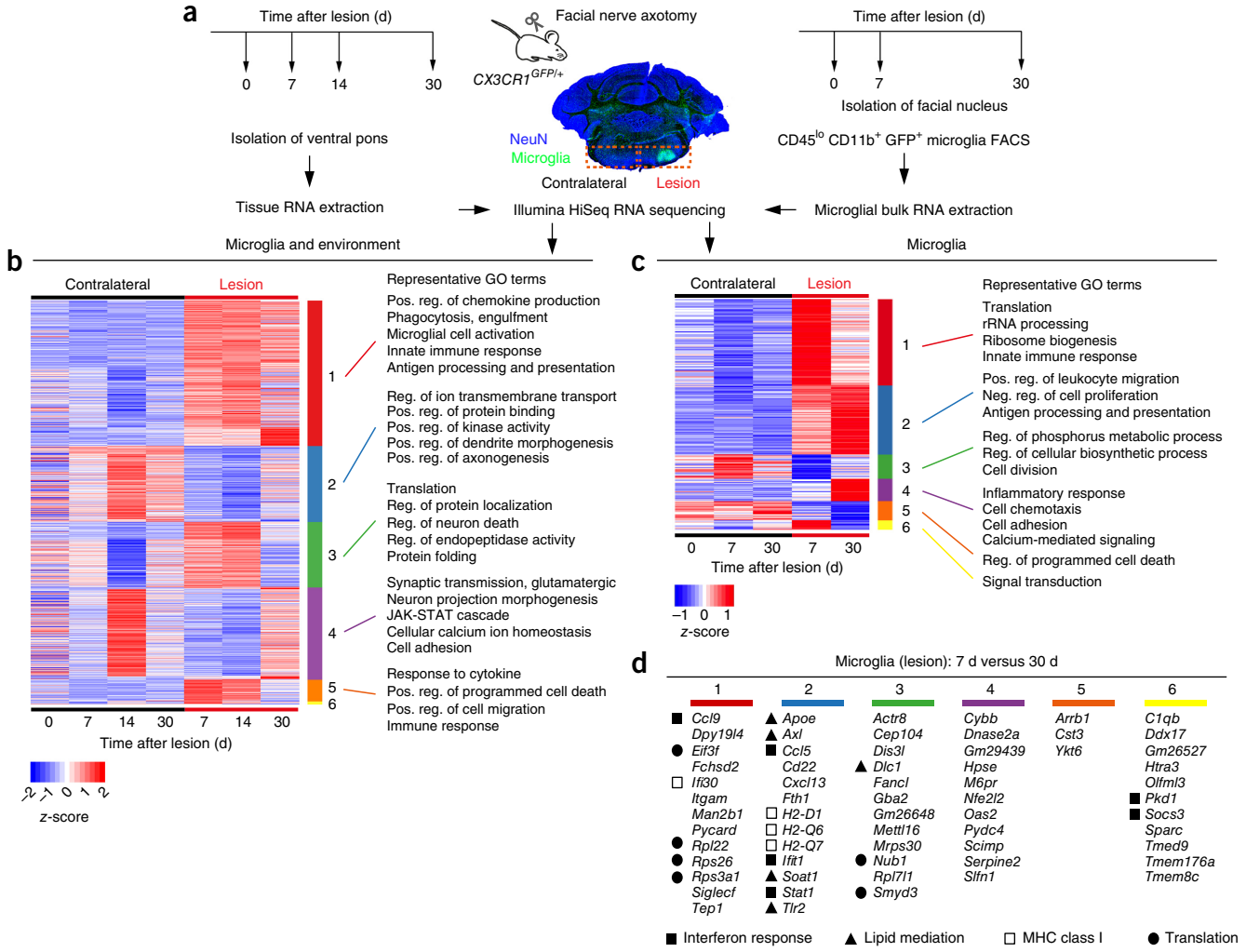

Figure 7 Resolution of excess microglia is accompanied by increased regulation of cell migration, interferon response and lipid mediation. (**a**) Scheme of gene expression analysis 7, 14 and 30 d after FNX in 8-week-old female *Cx3cr1*$^{GFP/+}$ mice. A coronal brain section 7 d after lesion is shown to indicate the region of the isolated whole ventral pons (orange dotted outline) containing the respective FN used for tissue RNA sequencing (left). The contralateral ventral pons from unoperated mice (0 d) was used as baseline control to account for possible gene regulation in the contralateral pons of unilaterally operated mice. Microglial cells from the respective FN 0, 7 and 30 d after FNX were obtained by FACS for bulk microglial RNA sequencing (right). (**b**) Heat map of differentially expressed genes (total 1,344) from the ventral pons that were significantly altered ($P < 0.05$) from at least one lesion group after FNX were sorted into six clusters (1, red; 2, blue; 3, green; 4, purple; 5, orange; 6, yellow). Representative Gene Ontology (GO) terms from the first five clusters are shown. The smallest cluster (yellow) contains ten genes. Color legend represents upregulation (red) and downregulation (blue) of genes based on $\log_2$ fold change. (**c**) Heat map of differentially expressed genes (total 257) from microglial cells that were significantly altered ($P < 0.05$) from at least one lesion group after FNX were sorted into six clusters. Representative GO terms from each cluster are shown. Color legend represents upregulation (red) and downregulation (blue) of genes based on $\log_2$ fold change. (**d**) Lists of differentially regulated microglia-expressed genes from the injured FN 7 and 30 d after FNX. Cluster color code corresponds to **c**. Known annotations of genes are indicated with symbols: filled square, response to interferon-α, interferon-β or interferon-γ; triangle, lipid mediation; open square, antigen processing and presentation of peptide antigen via MHC class I; circle, translation. $n = 3$ mice per group. Pos., positive; neg., negative; reg., regulation.

the decline in microglial cell numbers compared to the 7 d time point (**Fig. 5b** and **Supplementary Table 3**) and supports our observation of microglial cell egress from the site of injury (**Fig. 6d–f**). These results also suggest that injury resolution occurs about 1 month after FNX. In sum, the detected transcriptional changes provide a molecular basis for the observed kinetics of the microglial network during neurodegeneration, ranging from changes in microglial cell morphology, cell density and cell activation status to the resolution of gliosis.

DISCUSSION

In this study, our newly established microglia-focused multicolor reporter mouse model revealed the organization of the microglial network during health, disease and recovery (**Supplementary Fig. 5**). We found heterogeneous rates of microglial replenishment in different brain compartments that occurred in a context-dependent manner. We furthermore discovered selected clonal microglial expansion in response to local neuronal damage in the CNS. Notably, our model did not comprise experimentally induced microglial ablation[14,15,24] or widespread disease[30]. Our Microfetti model also allowed us to observe the restoration of microglial cell density by apoptotic cell death and egress, which were previously not possible to demonstrate *in vivo*.

Consensus from mouse studies states that adult microglia are yolk-sac-derived tissue macrophages that are long-lived and self-propagating[4,6,7,11,25,26,35]. Our data support this view. However, the variation in

region-associated cell proliferation frequencies recorded over at least 9 months shows that although the microglial compartment as a whole is independent of bone marrow input, most individual adult microglial cells do not uniformly display extended longevity. Both our fate-mapping study based on the Microfetti models and the integration of the thymidine analogs EdU and BrdU in dividing *Cx3cr1*^{GFP} microglial cells corroborated the heterogeneous rates of microglial renewal[28] and microglial cell densities[22] as a function of their microenvironment. Indeed, organ-specific macrophage identities were shown to be shaped by their repertoire of enhancer elements[36,37]. We found that microglia in the olfactory bulb, hippocampus and cerebellum had a higher rate of turnover than those in the cortex, midbrain and hypothalamus, which is in line with the elevated cerebellar and hippocampal immune vigilance reported recently[12]. In particular, we found that the rates of microglial turnover matched the turnover of other CNS cell types in the same regions, attributing a functional relevance to the heterogeneity of microglial renewal. Even in the olfactory bulb, where we observed a subpopulation of microglia that was more proliferative than microglia in other milieus, our analyses of the brains from Microfetti mice showed that bulbar microglia are not long-lived. A recent spatiotemporal fate analysis of zebrafish microglia claimed that embryo-derived microglia are short-lived and the brain macrophage population is supported by an alternative adult source[38]. However, neither our experimental setup nor the numerous fate-mapping studies[4–6,9,10,25,26] have demonstrated this in rodents.

Our results support a 'multipotency' view of endogenous adult microglia and do not support the existence of a transient amplifying type of CX_3CR1^+ microglia precursors in the healthy CNS, which has been speculated on but not formally demonstrated in several publications[14–16] in the absence of a multicolor fate-mapping mouse strain. First, we found no indication of any 'drift toward clonality' of microglia (which would have been indicated by large clusters of same-color cells at the end of our long-term study of TAM-induced adult Microfetti mice), as would be expected in a proposed stem cell model[32]. Second, microglial cell replication events were randomly distributed in all brain regions under homeostasis and in the injured FN at the peak of microgliosis. Taking these results together, we conclude that every individual CX_3CR1^+ microglial cell is plastic and possesses the replicative potential to divide and give rise to a clone.

The potential of all fully differentiated mature CX_3CR1^+ microglial cells to proliferate when necessary might be critical for mounting an immediate immune response to a challenge, as we have shown using the FNX model. We verified that microglial activation and proliferation occurred locally using immunohistochemistry for MHC class II and Ki67, as well as RNA sequencing. In the absence of significant changes in gene expression levels of microglia from the contralateral FN between healthy and FNX animals, any overall functional compensation or crosstalk in the contralateral ventral pons after FNX came from the tissue environment rather than from microglia, in contrast to differences reported in unilateral eye lesion models in rodents[39,40]. Using the calculations based on the Microfetti mouse model, we also excluded the recruitment of peripheral myeloid cells into the axotomized FN, as was previously demonstrated in axotomized mouse models with intact BBB that did not find infiltration of peripheral blood cells[18]. During chronic neurodegeneration in a mouse model of prion disease and also in the age-related Alzheimer's disease, microglial proliferation correlated with the severity of disease progression[30,31]. Our data suggest that the rapid activation and proliferation of microglia after FNX is not detrimental to the brain but necessary for reinstating tissue homeostasis within 2 months of injury. The critical time point and factors leading to microglial imbalance during mitigation of chronic diseases remain to be investigated.

The re-establishment of steady state microglial cell density to restore CNS homeostasis after the immune response was based not only on local apoptotic cell death, but also on cell egress to external pontine areas. The concept of macrophage emigration to the lymph nodes during resolution of inflammation[41] dominated the field until it was proposed that local apoptosis played a bigger role in the clearance of macrophages *in vivo*[42]. However, for microglia, we estimated that the rate of *in situ* microglial cell death (only significantly detected at 60 d after FNX) would not have sufficed as the only mechanism of recovery if apoptosis took place in a random and gradual manner over ~30 days. Gene expression analyses during the inflammation and resolution phases after FNX suggested that the process of recovery depends on the concerted coordination of a plethora of molecular and cellular events involving microglia and other CNS cell types. The overall upregulation of genes involved in lipid mediation at the onset of recovery (**Fig. 7d**) highlights the potential actions of lipid mediators in achieving tissue resolution[43] and should be further studied.

In conclusion, our study demonstrates that yolk-sac-derived microglia residing in the young adult brain are highly plastic immune cells that regulate the stability of their innate microenvironments in the CNS during health and disease.

METHODS

Methods, including statements of data availability and any associated accession codes and references, are available in the online version of the paper.

Note: Any Supplementary Information and Source Data files are available in the online version of the paper.

ACKNOWLEDGMENTS

The authors thank H. Snippert (University Medical Center Utrecht) and H. Clevers (Hubrecht Institute) for the *R26R*^{Confetti} mouse line, M. Follo and team at Lighthouse Fluorescence Technologies Core Facility, T. Blank for critical feedback, J. Bührer for technical support, and CEMT, University of Freiburg for excellent animal care. T.L.T. is supported by the German Research Foundation (DFG, TA1029/1-1) and Ministry of Science, Research and the Arts, Baden-Wuerttemberg (Research Seed Capital). M.P. is supported by the BMBF Competence Network of Multiple Sclerosis (KKNMS), the Sobek-Stiftung and the DFG (SFB992, SFB1140, Reinhart-Koselleck grant). F.F.-K., J.A.P., S.J., J.P. and M.P. are supported by the SFB/TRR167 "NeuroMac".

AUTHOR CONTRIBUTIONS

T.L.T. and M.P. conceived the study. T.L.T. established the methods. D.M., O.R. and T.L.T. designed the software and validated imaging data. T.L.T., J.D., F.F.-K., G.L., S., D.G., M.D., A.D., T.S., A.A.-F., O.S., A.M., A.S. and S.J. performed experiments and/or analyses. T.L.T., L.M.S., J.A.P., D.G., J.P., O.R. and M.P. provided supervision. T.L.T., D.M. and M.P. wrote the manuscript. All authors contributed to the editing of the paper.

COMPETING FINANCIAL INTERESTS

The authors declare no competing financial interests.

1. Hanisch, U.K. & Kettenmann, H. Microglia: active sensor and versatile effector cells in the normal and pathologic brain. *Nat. Neurosci.* **10**, 1387–1394 (2007).
2. Prinz, M. & Priller, J. Microglia and brain macrophages in the molecular age: from origin to neuropsychiatric disease. *Nat. Rev. Neurosci.* **15**, 300–312 (2014).
3. Ransohoff, R.M. & Perry, V.H. Microglial physiology: unique stimuli, specialized responses. *Annu. Rev. Immunol.* **27**, 119–145 (2009).
4. Ginhoux, F. *et al.* Fate mapping analysis reveals that adult microglia derive from primitive macrophages. *Science* **330**, 841–845 (2010).
5. Gomez Perdiguero, E. *et al.* Tissue-resident macrophages originate from yolk-sac-derived erythro-myeloid progenitors. *Nature* **518**, 547–551 (2015).

6. Hashimoto, D. *et al.* Tissue-resident macrophages self-maintain locally throughout adult life with minimal contribution from circulating monocytes. *Immunity* **38**, 792–804 (2013).
7. Hagemeyer, N. *et al.* Transcriptome-based profiling of yolk sac-derived macrophages reveals a role for Irf8 in macrophage maturation. *EMBO J.* **35**, 1730–1744 (2016).
8. Kierdorf, K. *et al.* Microglia emerge from erythromyeloid precursors via Pu.1- and Irf8-dependent pathways. *Nat. Neurosci.* **16**, 273–280 (2013).
9. Schulz, C. *et al.* A lineage of myeloid cells independent of Myb and hematopoietic stem cells. *Science* **336**, 86–90 (2012).
10. Sheng, J., Ruedl, C. & Karjalainen, K. Most tissue-resident macrophages except microglia are derived from fetal hematopoietic stem cells. *Immunity* **43**, 382–393 (2015).
11. Goldmann, T. *et al.* Origin, fate and dynamics of macrophages at central nervous system interfaces. *Nat. Immunol.* **17**, 797–805 (2016).
12. Grabert, K. *et al.* Microglial brain region-dependent diversity and selective regional sensitivities to aging. *Nat. Neurosci.* **19**, 504–516 (2016).
13. Shemer, A., Erny, D., Jung, S. & Prinz, M. Microglia plasticity during health and disease: an immunological perspective. *Trends Immunol.* **36**, 614–624 (2015).
14. Bruttger, J. *et al.* Genetic cell ablation reveals clusters of local self-renewing microglia in the mammalian central nervous system. *Immunity* **43**, 92–106 (2015).
15. Elmore, M.R.P. *et al.* Colony-stimulating factor 1 receptor signaling is necessary for microglia viability, unmasking a microglia progenitor cell in the adult brain. *Neuron* **82**, 380–397 (2014).
16. Sieweke, M.H. & Allen, J.E. Beyond stem cells: self-renewal of differentiated macrophages. *Science* **342**, 1242974 (2013).
17. Ajami, B., Bennett, J.L., Krieger, C., Tetzlaff, W. & Rossi, F.M.V. Local self-renewal can sustain CNS microglia maintenance and function throughout adult life. *Nat. Neurosci.* **10**, 1538–1543 (2007).
18. Mildner, A. *et al.* Microglia in the adult brain arise from Ly-6ChiCCR2+ monocytes only under defined host conditions. *Nat. Neurosci.* **10**, 1544–1553 (2007).
19. Mildner, A. *et al.* Distinct and non-redundant roles of microglia and myeloid subsets in mouse models of Alzheimer's disease. *J. Neurosci.* **31**, 11159–11171 (2011).
20. Davalos, D. *et al.* ATP mediates rapid microglial response to local brain injury *in vivo*. *Nat. Neurosci.* **8**, 752–758 (2005).
21. Nimmerjahn, A., Kirchhoff, F. & Helmchen, F. Resting microglial cells are highly dynamic surveillants of brain parenchyma in vivo. *Science* **308**, 1314–1318 (2005).
22. Lawson, L.J., Perry, V.H., Dri, P. & Gordon, S. Heterogeneity in the distribution and morphology of microglia in the normal adult mouse brain. *Neuroscience* **39**, 151–170 (1990).
23. Jung, S. *et al.* Analysis of fractalkine receptor CX_3CR1 function by targeted deletion and green fluorescent protein reporter gene insertion. *Mol. Cell. Biol.* **20**, 4106–4114 (2000).
24. Parkhurst, C.N. *et al.* Microglia promote learning-dependent synapse formation through brain-derived neurotrophic factor. *Cell* **155**, 1596–1609 (2013).
25. Goldmann, T. *et al.* A new type of microglia gene targeting shows TAK1 to be pivotal in CNS autoimmune inflammation. *Nat. Neurosci.* **16**, 1618–1626 (2013).
26. Yona, S. *et al.* Fate mapping reveals origins and dynamics of monocytes and tissue macrophages under homeostasis. *Immunity* **38**, 79–91 (2013).
27. Wieghofer, P., Knobeloch, K.P. & Prinz, M. Genetic targeting of microglia. *Glia* **63**, 1–22 (2015).
28. Lawson, L.J., Perry, V.H. & Gordon, S. Turnover of resident microglia in the normal adult mouse brain. *Neuroscience* **48**, 405–415 (1992).
29. Ajami, B., Bennett, J.L., Krieger, C., McNagny, K.M. & Rossi, F.M.V. Infiltrating monocytes trigger EAE progression, but do not contribute to the resident microglia pool. *Nat. Neurosci.* **14**, 1142–1149 (2011).
30. Gómez-Nicola, D., Fransen, N.L., Suzzi, S. & Perry, V.H. Regulation of microglial proliferation during chronic neurodegeneration. *J. Neurosci.* **33**, 2481–2493 (2013).
31. Olmos-Alonso, A. *et al.* Pharmacological targeting of CSF1R inhibits microglial proliferation and prevents the progression of Alzheimer's-like pathology. *Brain* **139**, 891–907 (2016).
32. Snippert, H.J. *et al.* Intestinal crypt homeostasis results from neutral competition between symmetrically dividing Lgr5 stem cells. *Cell* **143**, 134–144 (2010).
33. Wuidart, A. *et al.* Quantitative lineage tracing strategies to resolve multipotency in tissue-specific stem cells. *Genes Dev.* **30**, 1261–1277 (2016).
34. Ghigo, C. *et al.* Multicolor fate mapping of Langerhans cell homeostasis. *J. Exp. Med.* **210**, 1657–1664 (2013).
35. Alliot, F., Godin, I. & Pessac, B. Microglia derive from progenitors, originating from the yolk sac, and which proliferate in the brain. *Brain Res. Dev. Brain Res.* **117**, 145–152 (1999).
36. Gosselin, D. *et al.* Environment drives selection and function of enhancers controlling tissue-specific macrophage identities. *Cell* **159**, 1327–1340 (2014).
37. Lavin, Y. *et al.* Tissue-resident macrophage enhancer landscapes are shaped by the local microenvironment. *Cell* **159**, 1312–1326 (2014).
38. Xu, J. *et al.* Temporal-spatial resolution fate mapping reveals distinct origins for embryonic and adult microglia in zebrafish. *Dev. Cell* **34**, 632–641 (2015).
39. Gallego, B.I. *et al.* IOP induces upregulation of GFAP and MHC-II and microglia reactivity in mice retina contralateral to experimental glaucoma. *J. Neuroinflammation* **9**, 92 (2012).
40. Cen, L.P. *et al.* Bilateral retinal microglial response to unilateral optic nerve transection in rats. *Neuroscience* **311**, 56–66 (2015).
41. Bellingan, G.J., Caldwell, H., Howie, S.E., Dransfield, I. & Haslett, C. In vivo fate of the inflammatory macrophage during the resolution of inflammation: inflammatory macrophages do not die locally, but emigrate to the draining lymph nodes. *J. Immunol.* **157**, 2577–2585 (1996).
42. Gautier, E.L., Ivanov, S., Lesnik, P. & Randolph, G.J. Local apoptosis mediates clearance of macrophages from resolving inflammation in mice. *Blood* **122**, 2714–2722 (2013).
43. Schwab, J.M., Chiang, N., Arita, M. & Serhan, C.N. Resolvin E1 and protectin D1 activate inflammation-resolution programmes. *Nature* **447**, 869–874 (2007).

ONLINE METHODS

Mice. Female C57Bl/6J (wild-type), *Cx3cr1*$^{GFP/+}$ (ref. 23) and *Cx3cr1*$^{creER/+}$ *R26R*$^{Confetti/+}$ (named "Microfetti" in this study) mice were bred in specific-pathogen-free facility and given food and water *ad libitum*. *Cx3cr1*^{creER} (refs. 25,26) was genotyped by PCR using the forward primer 5′- CCT CTA AGA CTC ACG TGG ACC TG-3′ and the reverse primer 5′- GCC GCC CAC GAC CGG CAA AC-3′, which amplify a 304-bp product. Genotyping for *R26R*^{Confetti} (ref. 32) was according to Jackson Laboratory (stock no. 013731). All experiments were performed in a blinded manner by random assignment of numbers to mice, tissues and images for data acquisition and processing. Animal studies were approved by the Regional Councils of Freiburg and Berlin, Germany.

Administration of tamoxifen. Ten milligrams of tamoxifen (TAM, Sigma) were dissolved at 40 °C to 20 mg/ml in corn oil and applied subcutaneously in Microfetti mice.

Intravital imaging. A thin skull chronic cranial window was prepared over the parietal cortex[44] 4 weeks after TAM induction in Microfetti mice. The parietal bone was thinned over by consecutive passages of a drill until a thickness of 15–25 µm was reached. It was reinforced with a piece of cover glass glued to the bone with cyanoacrylate. A titanium ring was attached to the skull with dental cement to clamp the mouse's head to the microscope table during imaging. Surgery was performed under anesthesia with isoflurane (1.5–1.8% in 70% O_2, 30% N_2O). During surgery and until day 3 after surgery, carprofen (5 µg per g body weight) was administered intraperitoneally (i.p.), along with tramadol (2.5 mg per 100 ml drinking water), acetaminophen (200 mg per 100 ml drinking water) and cotrimoxazol (33.6 mg per 100 ml drinking water) until 1 week after surgery to ensure complete analgesia during the postoperative period.

Imaging was performed 2 weeks after surgery under isoflurane anesthesia. We employed a LaVision TriM Scope two-photon laser scanning microscope (LaVision Biotec) equipped with a tunable Ti:sapphire laser operating at 860 nm and pumping an optical parametric oscillator tuned to 1,080 nm. This setup was optimized for the detection of RFP$^+$ microglia and less so for CFP$^+$, GFP$^+$ or YFP$^+$ cells. To map RFP$^+$ microglial cells at consecutive time points, we scanned the entire cranial window (typically 2.25–3 mm^2), generating 350 µm × 350 µm tiles encompassing the cortex with a depth of ~200 µm. Second harmonic signal from the bone was acquired to stitch the tiles using a FIJI plug-in[45] and to provide landmarks to unequivocally identify RFP$^+$ microglia across different time points. To produce highly localized lesions under the cranial window, the Ti:sapphire laser beam was halted for 10–20 s on a single spot within the scanned volume. To image the dynamics of microglial processes, stacks encompassing whole microglial cells located 100–150 µm below the cortical surface were acquired at 1-min intervals over 30 min. For quantification, maximum intensity projection images were automatically thresholded and segmented in FIJI. The fractional change of the area covered by microglia in two-dimensional maximum intensity projections was calculated from the segmented images for each interval and averaged over the entire period of observation.

Administration of lipopolysaccharide (LPS). Wild-type and Microfetti mice received 4 mg per kg body weight of LPS (purified from *E. coli* 0127:B8, Sigma L3129, lot 064M4021V) dissolved in phosphate-buffered saline i.p. on days 1 and 3 before analysis on day 5 to induce microglial proliferation[46].

Facial nerve axotomy. Unilateral facial nerve transection at the stylomastoid foramen was performed in *Cx3cr1*$^{GFP/+}$ mice or 2 weeks after TAM application in Microfetti mice. Carprofen (5 µg per g body weight) was administered subcutaneously directly after the surgery. Successful nerve injury indicated by ipsilateral whisker paresis was assessed immediately upon recovery from mild anesthesia (i.p. 100 mg ketamine and 5 mg xylazine per kg body weight).

Flow cytometry and FACS. For characterization of Microfetti, microglial samples from Microfetti and age-matched wild-type mice were analyzed with the following markers: CD45-BV421 (BioLegend 103133), CD11b-BV605 (BioLegend 101237), CD44-Alexa Fluor 700 (BioLegend 103026), CD62L-Alexa Fluor 700 (BioLegend 104426), MHC class II-PE-Cy7 (BioLegend 107630), Ly6C-Alexa Fluor 700 (BD Pharmingen 561237) and CD115-PE-Cy7 (eBioscience 25-1152-82). Microglial cells were collected from a brain hemisphere using density gradient separation. Tissues were gently homogenized and strained through a 70-µm nylon filter (Fisher Scientific). After centrifugation, cells were resuspended in 37% isotonic Percoll (Sigma) and underlaid with 70% isotonic Percoll. The gradient was centrifuged at 800*g* for 30 min at 25 °C. Interface cells were collected and washed extensively in FACS buffer (PBS and 0.5% FCS) before antibody staining for 30 min at 4 °C. Compensation settings were determined using beads, blood from GFP or YFP transgenic mice and cell lines expressing DsRed or Cerulean. For analysis of proliferation in Confetti$^+$ and Confetti$^-$ microglial cells, surface marker staining was performed before fixation and permeabilization according to BD Cytofix/Cytoperm (BD Biosciences). Intracellular staining was done with a cocktail of Ki67-Alexa Fluor 647 (rat IgG2a isotype control BioLegend 400526), anti-GFP-Alexa Fluor 488 (BioLegend 338008) and rabbit anti-RFP (Thermo Fisher Scientific 710530), followed by Alexa 594-conjugated anti-rabbit IgG (Molecular Probes A11012). Cell suspensions were analyzed on the LSRFortessa (Becton Dickinson). Bulk microglia were collected in RNAprotect Cell Reagent (Qiagen) on a MoFlo Atrios EQ (Beckman Coulter). Data were analyzed with FlowJo 7.6.5 software.

Immunohistochemistry. Mice were anesthetized (i.p. 100 mg ketamine and 5 mg xylazine per kg body weight) and transcardially perfused with PBS followed by 4% paraformaldehyde in PBS. CNS and other organs were postfixed for 4–6 h at 4 °C, washed in PBS and incubated in 30% sucrose in PBS at 4 °C until fully submerged. All tissues were protected from light. Samples were embedded in OCT (Tissue-Tek) for frozen sectioning on a cryostat (Leica). To preserve the orientation of the injured facial nuclei and to allow proper storage of all coronal pontine sections for various subsequent marker analyses, 16-µm cryosections on slides were prepared from brains with unilateral lesions and kept at −20 °C until use. All other studies were performed on 50-µm free-floating sagittal brain sections. Tissues were rehydrated or permeabilized in blocking solution (0.1–0.5% Triton-X 100, 5% bovine albumin, normal goat or normal donkey serum and PBS) for 1 h at room temperature and incubated 16–48 h at 4 °C with the relevant primary antibodies diluted in 5% serum and PBS: 1:500 rabbit anti-Iba-1 (Wako 019-19741), 1:100 mouse anti-NeuN (Chemicon MAB377X), 1:40 goat anti-Olig2 (Santa Cruz sc-19969), 1:300 rat anti-CD31 (BD Pharmingen 550300), 1:5,000 rabbit anti-GFAP (Abcam ab7260), 1:1,000 sheep serum albumin (Abcam ab8940), 1:500 chicken anti-GFP (Abcam ab13970), 1:1,000 rabbit anti-Ki67 (Abcam ab15580), 1:100 mouse anti-MHC class II (Abcam ab23990) and 1:200 rat anti-Lamp2 (Abcam ab13524). Triton-X 100 was excluded in analyses involving Confetti colors to ensure better detection of native membrane-bound CFP (mCFP), which gives low signal. Extensive wash steps were performed with PBS. Sections were incubated at 1:1,000 with corresponding secondary antibodies conjugated to Alexa Fluor 488 (Life Technologies A-11008, A-11039, A-21208) or 647 (Life Technologies A-21235, A-21244, A-21447, A-21448) for 1–2 h at room temperature. Nuclear counterstain 4′,6-diamidino-2-phenylindole (DAPI, 1:5,000, Sigma) was included where required. Slices were mounted with ProLong Diamond Antifade Mountant (Life Technologies) or Mowiol (Sigma).

Triple labeling with EdU, BrdU and antibody. *Cx3cr1*$^{GFP/+}$ mice were given a single dose of 150 µg EdU in 100 µL PBS i.p.[47], followed by five consecutive daily i.p. pulses of 5 mg BrdU in 300 µL PBS starting 2 d later. For triple stain to label microglia or astrocytes, 50-µm mouse brain sagittal sections were permeabilized as described before, followed by DNA denaturation in 2 M HCl for 1 h at 37 °C. Sections were re-equilibrated in PBS at pH 8.5 and washed in PBS until they regained their usual appearance. Click-iT EdU (Invitrogen) staining was performed according to manufacturer's protocol for the Alexa Fluor 647 Imaging Kit. Samples were blocked for 30 min at room temperature before overnight incubation with 1:20 mouse anti-BrdU antibody (Roche 11170376001) at 4 °C. Brief washes with PBS were performed before overnight incubation with 1:500 chicken anti-GFP (Abcam ab13970) or 1:5,000 rabbit anti-GFAP (Abcam ab7260) at 4 °C for GFP-labeled microglia or astrocytes, respectively. Alexa Fluor 568-conjugated anti-mouse IgG (Life Technologies A-11004) and Alexa Fluor 488-conjugated anti-chicken IgY (Life Technologies A-11039) or anti-rabbit IgG (Life Technologies A-11008) were used at 1:1,000 for 2 h at room temperature for visualizing BrdU and GFP or GFAP. For triple stain to label immature neurons, permeabilization and Click-iT EdU staining was carried out followed by 1 h blocking at room temperature and 48 h incubation with 1:200 goat anti-doublecortin (Santa Cruz sc-8066) at 4 °C. Alexa Fluor 488-conjugated anti-goat IgG

doi:10.1038/nn.4547

(Life Technologies A-11055) was used. After washing, 2 M HCl treatment was done for 30 min at 37 °C, followed by the same procedure described for BrdU visualization. Sections were mounted with ProLong Diamond Antifade Mountant (Life Technologies). Five to eight sections were analyzed per brain.

TUNEL analysis. For terminal deoxynucleotidyl transferase dUTP nick-end labeling (TUNEL) of apoptotic microglial cells, the ApopTAG peroxidase *in situ* detection kit (Merck Millipore) was used in conjunction with an Alexa Fluor 647-conjugated anti-sheep IgG antibody (Life Technologies A-21448). Microglia were stained using rabbit anti-Iba-1 antibody (Wako 019-19741) and visualized by Alexa Fluor 488-conjugated secondary antibody (Life Technologies A-11008).

Confocal microscopy. All images used for analyses of Confetti colors with additional Iba-1 and DAPI stains were taken on the Olympus FluoView 1000 with a 20×, 0.95 NA W or 20×, 0.85 NA oil objective at 8 µs/pixel for 1,024 × 1,024 pixels in *xy*. The voxel size in *xyz* was 0.621 µm × 0.621 µm × 1.5 (facial nerve injury model) or 2 µm (homeostasis study). A common pinhole size of 80 µm was used. Two virtual channels were set up to excite mCFP, cytoplasmic YFP and Alexa Fluor 647 corresponding to the anti-Iba-1 label with 458 nm, 515 nm and 635 nm and to collect the emission signals at 466–495 nm, 521–561 nm and 655–755 nm, respectively, followed by excitation of DAPI, nuclear GFP (nGFP) and cytoplasmic RFP with 405 nm, 488 nm and 561 nm, with emission signals collected at 425–466 nm, 498–514 nm and 575–620 nm, respectively. *z* stacks for cortical analyses of Confetti$^+$ microglia density were randomly obtained from the posterior somatomotor, somatosensory and posterior parietal association areas, and anterior visual cortical nuclei. A minimum of three sections per region per brain of a Microfetti mouse were analyzed.

For TUNEL analysis, confocal images from both the injured facial nucleus (FN) and the contralateral nucleus were acquired with a Leica TCS SPE microscope encompassing 200 µm × 200 µm in *xy*. Iba-1$^+$ microglial cells containing TUNEL and DAPI-stained nuclei were counted in single confocal planes using Matlab-based custom software. For assessing Lamp2 coverage, confocal images of both FN encompassing 367 µm × 367 µm in *xy* were obtained. Lamp2 and Iba-1 signals were automatically thresholded from single confocal planes to calculate the fraction of Lamp2$^+$ area within the total Iba-1 immunoreactive area. For the quantification of Lamp2$^+$ Iba-1$^+$ microglial phagocytic cups, confocal images encompassing 738 µm × 738 µm in *xy* were obtained from the ipsilateral and contralateral pons. Three or four sections were analyzed per brain.

Fluorescence microscopy. *z* stacks of large brain regions of *Cx3cr1*$^{GFP/+}$ mice and whole pons of Microfetti mice after ipsilateral facial nerve transection were acquired on a Keyence BZ-9000 inverted fluorescence microscope using a 20×, 0.75 NA objective lens. Band-pass filters for CFP, YFP, RFP, Alexa Fluor 647 and DAPI were used for imaging tissues from Microfetti, omitting the collection of rare nGFP signals and bleed-through from YFP, to facilitate subsequent semi-automated cell detection.

Image analysis and processing. All experiments were performed in a blinded manner, as samples were assigned random numbers for data acquisition and processing. Simple quantification of GFP$^+$, Ki67$^+$ or MHC class II$^+$ microglial cells was done on Imaris software (Bitplane). For analyses of large brain areas, *z* stacks from the fluorescence microscope were stitched using XuvTools[48], followed by assignment of region of interest (ROI) and semiautomated microglial cell detection in three dimensions using a Matlab-based custom program. Cell detection in six-color confocal volumes of Microfetti samples was also processed and validated with the same platform.

Computational analysis. Every multichannel confocal image data set was represented as I_j, $j \in \mathbb{N}$. Indices of images that were taken from the same mouse m were pooled in sets $\mathcal{M}_m = \{i_1, \ldots, i_{N_m}\}$. Every image has a ROI R_j that delineates the valid image volume. Cell $i \in \{1, \ldots, N^j\}$ from image j has a location $\mathbf{c}_i^j \in \mathbb{R}^3$ and a label $l_i^j \in \{0, \ldots, 4\}$. The label indicates the channel in which the microglial cell was detected. $l = 0$ denotes that the cell was only visible in the Alexa Fluor 647 channel; that is, the microglial cell was stained by anti-Iba-1 antibody and did not express a Confetti reporter. For l = 1, 2, 3 or 4, the cell was also detected in the CFP, YFP, RFP or GFP channel, respectively.

To assess the clustering properties of recorded Confetti$^+$ microglial cells, we derived a Confetti$^+$ cell-centered density estimate of the number of same-colored cells in a ring of radius r and width w. The volume of the ring was defined by $V(r,w) = s_z^j \cdot 2rw\pi$, where s_z^j is the height of the stack from the image j in micrometers. This equation was considered valid only if the entire ring resided within the ROI of the image. If the ring was partially outside of the ROI, only the volume within was counted.

We let $\mathbf{c}_j^k$ be the location of a Confetti$^+$ microglial cell from image k; that is, $l_j^k \neq 0$. The density of same colored Confetti$^+$ microglial cells for a given radius and width of the ring was derived by dividing the number of these cells by the volume of the ring:

$$D\left(\mathbf{c}_i^k, r, w\right) = \frac{\left|\left\{\mathbf{c}_j^k \middle| r - \frac{1}{2}w \leq \left\|\mathbf{c}_i^k - \mathbf{c}_j^k\right\|_2 \leq r + \frac{1}{2}w,\ l_j^k = l_i^k \wedge j \neq i\right\}\right|}{V(r,w)} \quad (1)$$

The average Confetti$^+$ microglial cell density for all images corresponding to a single mouse m was obtained by averaging over the total number of densities for the given r,w of all images from one mouse. η is the total number of Confetti$^+$ microglial cells.

$$D_m(r,w) = \frac{1}{\eta} \sum_{j \in \mathcal{M}_m} \sum_{\{\mathbf{c}_i^j | l_i^j \neq 0\}} D\left(\mathbf{c}_i^j, r, w\right) \quad (2)$$

To compute the average density of Confetti$^+$ microglial cells for the entire experimental group or time point of analysis, we averaged over the number of mice analyzed per group. $\mathcal{E}$ contains the indices of mice for the experiment.

$$D_{\mathcal{E}}(r,w) = \frac{1}{|\mathcal{E}|} \sum_{m \in \mathcal{E}} D_m(r,w) \quad (3)$$

Plots of average Confetti$^+$ microglial cell densities per group or time point are shown as red lines (**Fig. 2e,f** and **Supplementary Fig. 2b**).

Monte Carlo (MC) simulation was performed to derive a baseline of random Confetti$^+$ microglial cell distributions (**Fig. 2e,f** and **Supplementary Fig. 2b**). Positions of Iba-1 labeled microglia were taken as fixed cell locations while the placement of Confetti$^+$ cells was randomized. Taking into account that each microglial cell could only express one Confetti reporter, the probability of a microglial cell from mouse m having a Confetti label a was given as

$$p(a \mid m) = \frac{\sum_{j \in \mathcal{M}_m} \left|\left\{l_i^j \middle| l_i^j = a, i \in \left\{1, \ldots, N^j\right\}\right\}\right|}{\sum_{j \in \mathcal{M}_m} N^j} \quad (4)$$

For each confocal data set, the simulation was run N_{MC} = 10,000 times. The Confetti$^+$ microglial cell densities for rings of radii $r \in$ {10 µm, 20 µm,…, 290 µm, 300 µm} and width w = 20 µm were computed using equation (3) for each instance. The resulting distributions of cell densities are presented in box plots, where the central mark is the median, the box encompasses the range from the 25th to 75th percentiles, and the whiskers represent the 2nd and 98th percentiles (**Fig. 2e,f** and **Supplementary Fig. 2b**). Points above the 98th percentile were considered outliers. When the red line representing measured data lies above the top whisker, the observation of clusters of same colored microglial cells could be considered a nonchance event, such as a result of cell proliferation.

For obtaining the nearest neighbor (NN) statistics of the total microglial cell population, the distance to the NN of a cell $\mathbf{c}_i^k$ was defined as

$$D_{\mathrm{NN}}\left(\mathbf{c}_i^k\right) = \min_j \left\|\mathbf{c}_i^k - \mathbf{c}_j^k\right\|_2,\ l_j^k = 0,\ i \neq j,\ j \in \left\{1, \ldots, N^k\right\} \quad (5)$$

The set of NN distances for an image k was given as

$$\mathcal{S}^k = \left\{D_{\mathrm{NN}}\left(\mathbf{c}_i^k\right) | i \in \left\{1, \ldots, N^k\right\}\right\} \quad (6)$$

We defined a statistical measurement $s_i : \mathcal{S}^k \mapsto \mathbb{R}$ as any mapping from the set of NN distances to the real numbers, where i enumerates the type of measurement; for example, i = 1, 2, 3, 4 or 5 denotes mean, median, maximum,

minimum or s.d., respectively. For each experiment we computed a measure $A^i_{\mathcal{E}}$ by obtaining the measurements for every image, averaging them across all images from each mouse, followed by averaging over the number of mice analyzed per group:

$$A^i_{\mathcal{E}} = \frac{1}{|\mathcal{E}|}\sum_{m\in\mathcal{E}}\frac{1}{|\mathcal{M}_m|}\sum_{k\in\mathcal{M}_m} s_i\left(\mathcal{S}^k\right) \tag{7}$$

To assess the spatial uniformity of sparse microglial cell proliferation events under steady state conditions, we first defined the location of a cell replication event as the point between two same color Confetti$^+$ microglial cells. Every pair of Confetti$^+$ microglial cells was taken to arise from a single replication event and was excluded from a subsequent count. Thus the set of proliferation events for an image k was defined as

$$\mathcal{P}_k = \left\{\frac{\mathbf{c}^k_i + \mathbf{c}^k_j}{2}\middle| l^k_i = l^k_j \wedge \left\|\mathbf{c}^k_i - \mathbf{c}^k_j\right\|_2 \leq 50\,\mu\text{m}\right\} \tag{8}$$

We used a kernel density estimation with a Gaussian kernel function $\sigma = 50$ to estimate the underlying distribution of the proliferation events

$$K_{\mathcal{E}} \sim \sum_{m\in\mathcal{E}}\sum_{k\in M_m}\sum_{\mathbf{c}\in\mathcal{P}_k}\mathcal{N}(\mathbf{c},\sigma) \tag{9}$$

All locations of proliferation from all images k pertaining to a set of results from the same brain region and time point were aggregated. The computation was performed on a discretized grid with 636 × 636 pixels. After the kernel density estimation, the pixel-wise difference of the estimated distribution to the uniform distribution was calculated. The s.d. derived from these measurements shows how far the estimated distribution of the proliferation events derived from the experiments is from the uniform distribution. To account for the relatively low sample counts in the steady state data sets, we performed a MC simulation to assess the uniformity of the measured distribution. For each MC iteration, we randomly sampled the measured number of proliferation events from a two-dimensional (2D) uniform distribution. A kernel density estimation as described above was performed to compute the s.d. to the uniform distribution. We performed $N_{\text{MC}} = 10{,}000$ iterations to obtain a distribution of simulated s.d. values arising from a 2D uniform distribution.

RNA sequencing and analysis. A rodent brain matrix (RBM-2000C, ASI Instruments) was used to obtain consistent coronal sections of pons containing both facial nuclei of *Cx3cr1*$^{GFP/+}$ mice after unilateral facial nerve axotomy. Total tissue RNA was column purified using the RNeasy Mini Kit (Qiagen) from the ipsilateral and contralateral ventral pons (containing the facial nucleus and parts of the gigantocellular reticular nucleus, intermediate reticular nucleus, parvicellular reticular nucleus α and spinal trigeminal nucleus oral). Library was prepared with the TruSeq mRNA Sample Prep kit (Illumina). Bulk microglial RNA was extracted from FACS-purified microglia of the facial nuclei using the RNeasy Plus Micro Kit (Qiagen). cDNA was prepared using the SMART-Seq v4 Ultra Low Input RNA Kit (Clontech). A library was generated with a Nextera XT (Illumina) custom small-sample protocol. Illumina HiSeq deep sequencing was carried out with 50-base single-read sequencing that generates 30–35 million reads per sample. Reads were aligned to the mouse genome using hisat2 (ref. 49) and the exon junctions were provided using the --raw-juncs option. The GRCm38 assembly from Ensembl was used for the genome fasta file with the annotations based on release 85 (Mus_musculus.GRCm38.82). Read counts per gene were quantified using Rsubread[50]. Differential gene expression was called between the contralateral side and lesion side in both tissue and bulk microglial RNA sequencing data using DESeq2 (ref. 51). Pairwise comparisons between the contralateral and lesion sides was performed for each time point. Genes with false discovery rate (FDR) < 0.05 were considered to show significant differential gene expression. All the significant genes at each time point were identified. For tissue data, significant changes in $\log_2$(fold change) across time points was tested following the model in DESeq2: counts ~ time point * side (where side can be either lesion or contralateral), against the null model: counts ~ time point + side. In both models, ~ indicates that the response variable on the left of the equation can be explained by the variables on the right. Independent variables such as time point and side are indicated by + in the null model. The interaction between the variables time point and side are denoted by * in the test model. Genes that showed a significant time effect (FDR < 0.05) were subsequently clustered using k means**.** Genes that did not show significant time effect were split into two groups, namely overall upregulated or overall downregulated, based on their mean $\log_2$(fold change). For bulk microglia analysis, we clustered all genes that were significant in at least 1 time point using k means. Gene Ontology (GO) term enrichment for each cluster was performed with topGO[52].

Statistical analysis. No statistical methods were used to predetermine sample sizes, but our sample sizes are similar to those previously reported[11,25,32–34]. Data distribution was assumed to be normal, but this was not formally tested for all experiments. GraphPad Prism5 was used for the following statistical tests. Comparisons between two groups were made by one-way ANOVA, Mann–Whitney U-test or Wilcoxon signed rank test for paired groups. Multiple comparisons were evaluated using two-way ANOVA with Bonferroni correction. Differences were considered statistically significant at $P < 0.05$. Data are presented as mean ± s.e.m. unless indicated otherwise.

A **Supplementary Methods Checklist** is available.

Code availability. Code for the image and gene expression analyses are available in the **Supplementary Software**.

Data availability. Accession codes: Gene Expression Omnibus, GSE79252 (tissue RNA sequences). European Nucleotide Archive: PRJEB18711 (microglial RNA sequences). The remaining data that support the findings of this study are available from the corresponding authors upon reasonable request.

44. Drew, P.J. *et al.* Chronic optical access through a polished and reinforced thinned skull. *Nat. Methods* **7**, 981–984 (2010).
45. Preibisch, S., Saalfeld, S. & Tomancak, P. Globally optimal stitching of tiled 3D microscopic image acquisitions. *Bioinformatics* **25**, 1463–1465 (2009).
46. Shankaran, M. *et al.* Measurement of brain microglial proliferation rates in vivo in response to neuroinflammatory stimuli: application to drug discovery. *J. Neurosci. Res.* **85**, 2374–2384 (2007).
47. Salic, A. & Mitchison, T.J. A chemical method for fast and sensitive detection of DNA synthesis in vivo. *Proc. Natl. Acad. Sci. USA* **105**, 2415–2420 (2008).
48. Emmenlauer, M. *et al.* XuvTools: free, fast and reliable stitching of large 3D datasets. *J. Microsc.* **233**, 42–60 (2009).
49. Kim, D., Langmead, B. & Salzberg, S.L. HISAT: a fast spliced aligner with low memory requirements. *Nat. Methods* **12**, 357–360 (2015).
50. Liao, Y., Smyth, G.K. & Shi, W. The Subread aligner: fast, accurate and scalable read mapping by seed-and-vote. *Nucleic Acids Res.* **41**, e108 (2013).
51. Love, M.I., Huber, W. & Anders, S. Moderated estimation of fold change and dispersion for RNA-seq data with DESeq2. *Genome Biol.* **15**, 550 (2014).
52. Alexa, A. & Rahnenfuhrer, J. TopGO: enrichment analysis for gene ontology. R package version 2.26.0 (2016).

doi:10.1038/nn.4547

Microglial confetti party

Charlotte Madore, Caroline Baufeld & Oleg Butovsky

Microglia are highly heterogeneous and plastic. However, the dynamics of their turnover have been difficult to visualize. A new multicolor reporter system reveals a plastic but stable network of microglia during health and disease.

One of the biggest challenges in the field of microglial research has been understanding how they self-renew at steady state and, more importantly, under pathological conditions. The ability to target microglia versus recruited monocytes in disease conditions remains a central step in devising appropriate therapy. Microglia arise from an embryonic origin that differs from that of peripheral myeloid populations[1,2]. Unlike monocytes, which are renewed throughout life from bone marrow hematopoietic stem cells, resident microglial cells in the healthy adult brain persist during adulthood via self-renewal, and this occurs without turnover from circulating blood progenitors[1,3–5]. In this issue of *Nature Neuroscience*, Tay *et al.*[6] identify the dynamics of microglial renewal in health and disease. Microglia are shown to self-renew stochastically in the healthy brain and expand clonally during pathology. The resulting excess in microglia is resolved by cell egress and programmed cell death.

Manipulation of resident microglia numbers has shown that they recover rapidly from resident proliferative sources after genetic ablation[7] or pharmacological depletion[8]. Thus, microglia resemble other tissue-resident macrophages, which self-renew during homeostasis[9]. However, mouse models such as *Cx3cr1*-promoter-based reporter mice have not enabled us to differentiate resident microglia from their progeny or even from their potential precursors, especially in disease[3,10,11].

Charlotte Madore, Caroline Baufeld and Oleg Butovsky are at the Ann Romney Center for Neurologic Diseases, Department of Neurology, Brigham and Women's Hospital, Harvard Medical School, Boston, Massachusetts, USA. Oleg Butovsky is at the Evergrande Center for Immunologic Diseases, Brigham and Women's Hospital, Harvard Medical School, Boston, Massachusetts, USA.
e-mail: obutovsky@rics.bwh.harvard.edu

In disease conditions, it has been even harder to distinguish the relative contributions of microglia and recruited monocytes. Ajami *et al.*[3] used a parabiosis-and-irradiation model to label circulating monocytes and found little or no contribution of peripheral monocytes to the microglial population in disease. However, no one has been able to dissect microglial renewal in disease.

Tay *et al.*[6] used an innovative method of fate-mapping brain microglia *in vivo* to visualize the dynamics with which microglial regulate their cell numbers in response to changes in their microenvironment. The authors found that under physiological conditions, the microglial network remains stable, self-proliferating in a stochastic manner at turnover rates that varied by region. However, in an acute model of neurodegeneration, facial nerve axotomy, microglia shifted from random proliferation to selective clonal expansion. The authors also found that the density and distribution of the original microglial network were restored by specific apoptosis.

To distinguish microglial subsets in the parenchyma without compromising the blood–brain barrier, the authors generated a myeloid-cell-specific multicolor reporter mouse line by crossing *Cx3cr1*^{creER} mice with a ubiquitously expressing *R26R*^{Confetti} model. The use of Cre-ER technology allows the authors to induce recombination leading to the expression of fluorescent proteins at a given time and in a cell-specific manner. In this technique, Cre recombinase is fused to a mutated ligand-binding domain of the human estrogen

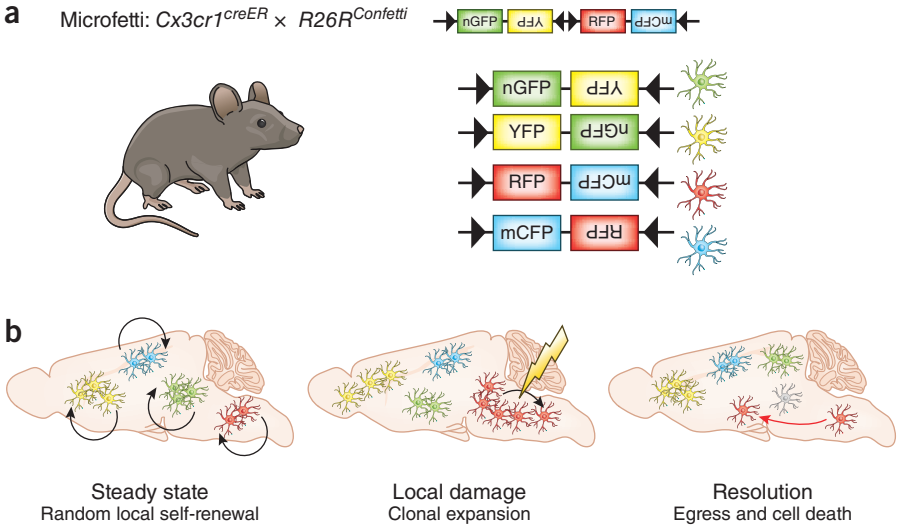

Marina Corral Spence/Springer Nature

Figure 1 Microglial network regulation in health and disease. (**a**) The Confetti reporter strain crossed with a myeloid-cell-specific Cre line generates the Microfetti mouse. It allows random multicolor labeling of microglia with one of four fluorescent proteins: nuclear green fluorescent protein (nGFP), cytoplasmic yellow fluorescent protein (YFP), cytoplasmic red fluorescent protein (RFP) and membrane-localized cyan fluorescent protein (mCFP). (**b**) This model reveals random local self-renewal of microglia in steady-state conditions. Local damage induces microgliosis through clonal expansion at the site of the lesion, which resolves by egress (red arrow) and apoptosis (gray cell) of excess cells to restore the resting microglia network.

receptor (ER) that is activated specifically by tamoxifen and not by estradiol. After induction of recombination by tamoxifen injection, $CX3CR1^{+}$ microglia randomly express one of four possible fluorescent reporter proteins encoded by the Confetti construct, enabling specific, long-term labeling of microglia and their daughter cells (**Fig. 1**). They named the resulting mouse line Microfetti.

By combining the Microfetti mouse with mathematical modeling, the authors were able to analyze the microglial network during homeostasis and demonstrate considerable microglial stability in the adult brain more than 36 weeks after recombination. In specific niches of cell proliferation, such as the hippocampus and olfactory bulb, the authors found subpopulations of microglia with increased self-renewal. This is in accordance with the findings of Askew *et al.*[5]; however, that study compromised the blood–brain barrier and led to the potential infiltration of blood monocytes.

Tay *et al.*[6] also provide insight into the dynamics of the microglia network *in vivo* during disease and recovery. The authors examined microglial dynamics after facial nerve axotomy, a neurodegenerative model that does not compromise the blood–brain barrier. Using this model, they observed the random self-renewal of steady state microglia shifting toward clonal expansion in response to an acute lesion. Microglia rapidly proliferated and formed a cluster of daughter cells as early as 2 days after the damage, which explains the microgliosis observed after facial nerve axotomy. The Microfetti technique excluded the possibility that microglia were recruited from elsewhere in the brain, as that would have led to a more random distribution of the labeled cells. The resolution of microgliosis was accompanied by a decrease in microglial density. Tay *et al.*[6] suggest that the homeostatic microglial network is restored by a combination of random microglial movement into nearby compartments and local apoptosis in the area of the lesion.

Finally, Tay *et al.*[6] characterized gene expression in clonally expanded microglia during the progression of neural injury. They found that during lesion progression on the way to resolution of microgliosis, the most-modulated microglia functions are related to phagocytosis, cell migration and immune responses such as antigen presentation.

This study provides a new perspective on microglial network regulation in health and especially in disease. Indeed, along with the previous dogma that microglia in rodents are long-lived cells and the recent view that they are self-renewing in steady-state conditions[12], Tay *et al.*[6] demonstrate that microglia renewal dynamics are highly dependent on their microenvironment and are region-specific within the CNS. The Microfetti model is a notable tool that confirms microglial plasticity and heterogeneity, and it shows that their density and rate of renewal vary in a context-dependent manner. More importantly, it demonstrates that microglia clonally expand while mounting an inflammatory response to local damage and then die or migrate to resolve the resulting microgliosis.

COMPETING FINANCIAL INTERESTS
The authors declare no competing financial interests.

1. Ginhoux, F. *et al. Science* **330**, 841–845 (2010).
2. Gomez Perdiguero, E. *et al. Nature* **518**, 547–551 (2015).
3. Ajami, B., Bennett, J.L., Krieger, C., Tetzlaff, W. & Rossi, F.M. *Nat. Neurosci.* **10**, 1538–1543 (2007).
4. Kierdorf, K. *et al. Nat. Neurosci.* **16**, 273–280 (2013).
5. Askew, K. *et al. Cell Rep.* **18**, 391–405 (2017).
6. Tay, T.L. *et al. Nat. Neurosci.* **20**, 793–803 (2017).
7. Bruttger, J. *et al. Immunity* **43**, 92–106 (2015).
8. Elmore, M.R. *et al. Neuron* **82**, 380–397 (2014).
9. Hashimoto, D. *et al. Immunity* **38**, 792–804 (2013).
10. Jung, S. *et al. Mol. Cell. Biol.* **20**, 4106–4114 (2000).
11. Parkhurst, C.N. *et al. Cell* **155**, 1596–1609 (2013).
12. Perry, V.H. & Teeling, J. *Semin. Immunopathol.* **35**, 601–612 (2013).
12. Nasr, S. *et al. J. Neurosci.* **31**, 13771–13785 (2011).

A cell-type-specific jolt for motor disorders

Yu-Wei Wu & Jun B Ding

Manipulating the activity of a subpopulation of external globus pallidus neurons with optogenetic deep brain stimulation ameliorates motor deficits in a mouse model of Parkinson's disease.

The motor symptoms of Parkinson's disease are primarily caused by the loss of nigrostriatal dopaminergic neurons, which leads to prominent motor deficits including akinesia or bradykinesia, tremors and muscular rigidity. In the past decade, deep brain stimulation (DBS), a surgical intervention targeting nuclei of the basal ganglia with high-frequency electrical pulses, has been shown to ameliorate motor deficits in Parkinson's disease. The internal globus pallidus, which is involved in the basal ganglia direct pathway, and the subthalamic nucleus (STN) are the primary targets of DBS[1]. In this issue of *Nature Neuroscience*, Mastro *et al.*[2] identify distinct neural populations in the external globus pallidus (GPe), a relay nucleus of the basal ganglia indirect pathway, that can restore movement in a Parkinson's disease mouse model when targeted by optogenetic DBS.

The neural circuits of the basal ganglia are composed of two main pathways. The striatal projection neurons of the direct pathway express the D1 dopamine receptor and project directly to the substantia nigra pars reticulata (SNr), the output nuclei of the basal ganglia, while the striatal projection neurons of the indirect pathway form multisynaptic connections to the output nuclei through the GPe (**Fig. 1a**)[3]. Using a mouse model of acute dopamine depletion combined with genetic strategies, optogenetic stimulation and single-unit recording, the authors demonstrated that transiently interfering with the activity of a subpopulation of GPe neurons induced long-lasting recovery of movement in dopamine-depleted mice. Mechanistically, this approach reversed the pathological spiking patterns in the SNr, not only during the optogenetic stimulation but also for hours afterward. Intriguingly, these effects could only be achieved by manipulating a particular subset of GPe neurons and not by global GPe stimulation. This discovery highlights the heterogeneous nature of GPe neurons, whose distinct functions have not been taken into consideration in the currently accepted functional and anatomical basal ganglia circuit model.

Synchronization of neural activity between STN and GPe—due to their reciprocal connections[4]—is a signature of Parkinson's disease[5]. Although the precise mechanism of DBS remains to be elucidated, one working hypothesis is that therapeutic DBS could disrupt pathological synchronization between STN and GPe. While stimulating STN has been demonstrated to improve motor symptoms[6], targeting GPe is

Yu-Wei Wu and Jun B. Ding are in the Department of Neurosurgery and the Department of Neurology and Neurological Sciences, Stanford University School of Medicine, Palo Alto, California, USA.
e-mail: dingjun@stanford.edu